Colloids and Surfaces A: Physicochemical and Engineering Aspects 688 (2024) 133529

Contents lists available at ScienceDirect

Colloids and Surfaces A: Physicochemical and Engineering Aspects

journal homepage: www.elsevier.com/locate/colsurfa

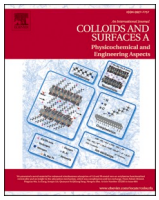

Natural and synthetic plagioclases: Surface charge characterization and sorption of trivalent lanthanides (Eu) and actinides (Am, Cm)

J. Lessing [a,1], J. Neumann [a,2,3], J. Lützenkirchen [b,4], F. Bok [a,5], S. Moisei-Rabung [b], D. Schild [b,6], V. Brendler [a,7], T. Stumpf [a,8], M. Schmidt [a,*,9]

[a] Helmholtz-Zentrum Dresden-Rossendorf (HZDR), Bautzner Landstraße 400, Dresden 01328 Germany
[b] Karlsruher Institut für Technologie (KIT), Hermann-von-Helmholtz-Platz 1, Eggenstein-Leopoldshafen 76344, Germany

GRAPHICAL ABSTRACT

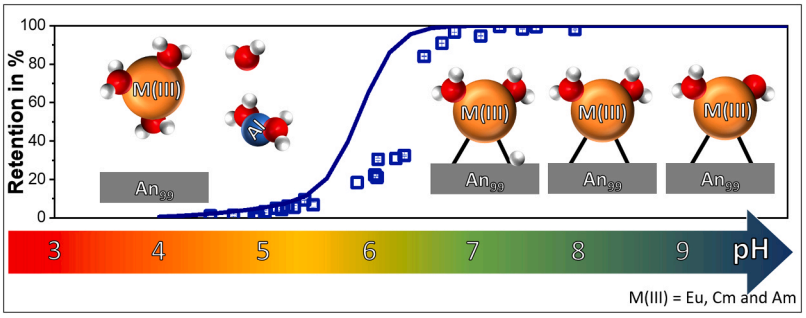

ARTICLE INFO

Keywords:
Ca-feldspar
Anorthite
Sorption
Trivalent metal ions
TRLFS
Surface Complexation Model
Charge Reversal

ABSTRACT

The environmental fate of radiotoxic actinides may be controlled by their interactions with feldspars. Here, the sorption of trivalent minor actinides (Am, Cm) and their rare earth analog Eu onto synthetic pure Ca-feldspar (anorthite) and natural plagioclases of different Ca contents is investigated, covering ranges of [M^{3+}] (52 nM–10 μM), solid-liquid ratios (1–3 g/L), pH (3–9), and ionic strengths (0.01–0.1 M NaCl) under both ambient and CO_2-free conditions. As a first step to understand the uptake behavior of the heavy metals, the hitherto unknown surface charge and (de-)protonation reaction of Ca-feldspars is characterized. The zeta potential shows an unusual increase and charge reversal between pH 4 and 7 , which becomes more pronounced with increasing amounts of Ca in the crystal lattice and is likely connected to adsorption and/or surface

* Corresponding author.
E-mail address: moritz.schmidt@hzdr.de (M. Schmidt).
[1] ORCID: 0000-0002-6485-4035
[2] *Current Address: Chemical Science and Engineering Division, Argonne National Laboratory, 9700 South Cass Ave, Lemont, IL 60439, USA*
[3] ORCID: 0000-0002-3650-3967
[4] ORCID: 0000-0002-0611-2746
[5] ORCID: 0000-0002-6885-2619
[6] ORCID: 0000-0001-6034-8146
[7] ORCID: 0000-0001-5570-4177
[8] ORCID: 0000-0002-4505-3865
[9] ORCID: 0000-0002-8419-0811

https://doi.org/10.1016/j.colsurfa.2024.133529
Received 21 December 2023; Received in revised form 13 February 2024; Accepted 21 February 2024
Available online 24 February 2024

precipitation of dissolved Al^{3+}. Streaming potential measurements yield (de)protonation constants for anorthite surface sites of log $K^{-} = -6.94 \pm 0.38$ and log $K^{+} = +6.84 \pm 0.38$. Batch sorption data shows strong immobilization of M^{3+} by plagioclases at mildly acidic and basic pH. Time-resolved laser fluorescence spectroscopy using Cm indicates the formation of an inner-sphere complex and its two hydrolyzed forms. The complex reactivity of dissolved Al^{3+} at the plagioclase-water interface severely complicated the development of a surface complexation model, emphasizing the need for additional research in this area. Our study highlights the importance of molecular-level studies to understand surface reactions and uncover unknown processes, which may have significant impact on the transport of (radiotoxic) contaminants in the geosphere.

1. Introduction

Spent nuclear fuel will remain highly radiotoxic over hundreds of thousands of years [1]. Worldwide, deep geological repositories are considered the safest disposal option on these geological time scales, when multi-barrier concepts, consisting of technical, geotechnical, and geological barriers, are implemented to minimize the release of radionuclides from the repository [2]. The geological barrier will be provided by a suitable host rock formation, typically clay, rock salt, or crystalline rocks [3,4]. Currently, concepts for the latter are the most developed, with construction for a first nuclear waste disposal scheduled to begin in Finland in 2024 [5]. Other countries also consider crystalline rock as a suitable host rock, for instance Sweden [5–7], Germany, the USA, Russia, China, Czech Republic, and Japan [3,7–12].

Crystalline rocks mainly consist of quartz, mica, and feldspar in varying compositions depending on their orogenesis. Feldspars belong to one of the most ubiquitous mineral group in the earth's crust [13]. They are aluminum tectosilicates and consist of AlO_4 and SiO_4 tetrahedra. Due to the substitution of Si^{4+} by Al^{3+}, the crystal lattice is negatively charged, which is compensated by cations, typically Na^{+}, K^{+}, or Ca^{2+}. The pure feldspar endmembers $CaAl_2Si_2O_8$ (anorthite, An), $NaAlSi_3O_8$ (albite, Ab), and $KAlSi_3O_8$ (orthoclase, Or) exist only in minor amounts in nature. Instead, solid solutions are commonly found between An and Ab (plagioclases), and Ab and Or (alkali feldspars). Large differences in the ionic radii of K^{+} ($r_K^{VI} = 138$ pm) and Ca^{2+} ($r_{Ca}^{VI} = 100$ pm) [14] and the different cationic charges result in a miscibility gap between Or and An [15].

The radiotoxicity of spent nuclear fuel after the decay of short-lived fission products is dominated by minor actinides, e.g., Americium (Am) and Curium (Cm), as well as Plutonium (Pu) [16]. Am and Cm are most stable in the trivalent oxidation state, and due to the expected reducing conditions in the repository, Pu is also likely to be present in significant amounts as Pu(III) [17,18]. In studies regarding the mobility of trivalent actinides in the environment, Eu^{3+} is often used as a non-radioactive and less toxic lanthanide analog [19–22]. Additionally, Eu^{3+} and Cm^{3+} show extraordinary luminescence properties, making them suitable for spectroscopic investigations of the structures of sorption complexes on a molecular level [22–26].

The fate of radionuclides in the environment is strongly influenced by their interactions with charged mineral surfaces, with inner-sphere (IS) and outer-sphere (OS) adsorption as two major immobilization mechanisms. For reliable risk assessments of final repositories for radioactive waste, thermodynamic data for sorption processes based on experimentally determined molecular structures of formed complexes are desirable, which can be applied for more robust modeling of reactive transport [27,28]. Yet, static distribution coefficients (K_d) that are only valid for specific geochemical conditions are still commonly used to describe the ratio of radionuclide concentration in the aqueous and on the solid phase. As one modern approach to overcome that problem, the mechanistic Smart-K_d concept was developed [29], which provides K_d matrices for a broad range of geochemical conditions. Comprehensive thermodynamic sorption data sets are needed to cover the full complexity of the systems relevant for the risk assessment of a repository. Fully coupled geochemical-transport codes exist, but on the scale of performance assessment calculations the solution and interfacial chemistries are strongly simplified because of the computational costs. A significant reduction in CPU time can, for example, be achieved by using simple interfacial models in terms of the electrical double layer (EDL). The use of the purely diffuse double layer (DDL) model avoids complications arising from the need to include ion-specificity in multilayer models and can be seen as a compromise between the entirely conditional K_d approach and the molecular level oriented CD-MUSIC approach. Despite the shortcomings of the DDL approach, it has been used in database development for ferrihydrite [30], manganese oxide [31], goethite [32], and gibbsite [33], and is actively used in environmental applications. Concerning databases the double layer models diminish problems of parameter incompatibilities of the more detailed models due to the absence of charge distribution factors, background electrolyte binding constants, or capacitance values. For all these reasons, in the present work, we use this simple model and attempt to include molecular level information from laser spectroscopic experiments.

The uptake of trivalent actinides and lanthanides on alkali feldspars has previously been investigated by several groups. Stumpf et al. [34] investigated the sorption of Cm^{3+} on Or and Ab using time-resolved laser-induced fluorescence spectroscopy (TRLFS). An IS species as well as its hydrolyzed form both with a luminescence lifetime of 107 ± 3 µs were found, corresponding to five remaining water molecules in the first coordination sphere of Cm [34]. Later, Li et al. investigated the impact of pH, temperature, concentration of organic matter, and counter ions on the sorption quantity of Eu^{3+} on K-feldspar using batch sorption experiments, showing that the presence of humic acids enhanced uptake of Eu^{3+} at low pH [35]. Recently, we have provided a large set of structural and thermodynamic data for the sorption of rare earth elements (Eu, Nd, La, Lu) and trivalent actinides (Am, Cm) on K-feldspar, which in this case is a mixture of Or and microcline, combining surface charge characterization, batch sorption experiments, and TRLFS. The combined experimental results were used to develop a generic surface complexation model (SCM), which accurately predicts independently reported sorption data of rare earth elements and trivalent actinides on K-feldspar [36].

While sorption of M^{3+} on Ab and Or was reported to be similar [34], quantitative comparisons of the sorption of metal ions onto alkali feldspars and plagioclases are extremely rare. The Al:Si ratio in the crystal lattice changes from 1:3 for alkali feldspars to 1:1 for An, which impacts mineral dissolution, surface charge, and available binding sites for sorption processes. Therefore, experimental data is needed to understand differences in reactivity between alkali feldspars and plagioclase minerals. Currently, only very few studies for the sorption of lanthanides or trivalent actinides onto plagioclases are available [37]. One study compared three different feldspars (microcline, Ab, and An) and reported no significant differences in the distribution coefficients of Am^{3+}, albeit for a very limited range of geochemical conditions (artificial groundwater at ambient temperature and pH 7.2–8.5) [38]. The study reports no spectroscopic or structural data on the surface complexes.

Here, we extend our previous study on K-feldspar[36] towards plagioclases with different Na:Ca ratios (denoted as An_x, where x is the mole fraction of Ca in percent). The aim of this study is to systematically compare M^{3+} uptake between alkali feldspars and plagioclases in respect to metal retention quantity as well as molecular adsorption

structures. First, we use electrophoretic mobility and zeta potential measurements for surface charge characterization of natural plagioclases and synthetic An. Second, we quantify sorption of M(III) on plagioclases by batch sorption experiments and identify the surface complexes by TRLFS using Cm. Attempts to extend the previously developed SCM towards Ca-feldspar based on the new experimental data highlight the complexity arising from the higher solubility of plagioclases in comparison to alkali feldspars.

2. Materials and methods

2.1. Materials

Labradorite (An_{79}, Sugarloaf Peak, Australia) was obtained from the Mineraliensammlung (mineral collection) at TU Bergakademie Freiberg (Germany). Oligoclase (An_{23}) was purchased from Ward's Science Company (USA). Anorthite (An_{99}) was synthesized following a route established by Chihara et al. [39]. In brief, $CaCO_3$ (p.a., Merck), Al_2O_3 (99.99%, Alfa Aesar), and SiO_2 (99.95%, Merck) were mixed stoichiometrically with a molar ratio of 1:1:2. This mixture was sintered at 1500 °C for 50 h.

The crystal structures of the natural and synthesized minerals were analyzed by powder X-ray diffraction (PXRD, Rigaku MiniFlex600 PDXL). X-ray fluorescence spectroscopy (PANalytical, Axios^{mAX}, Rh X-ray Source) was applied to determine the exact amounts of Al, Si, Na, K, and Ca (Table 1) to identify each mineral's composition and confirm the mineral assignments. The preparation procedure included crushing the minerals in an agate ball mill and subsequent sieving to a grain size of < 63 μm. Specific surface areas (SSAs) of the mineral powders were determined via multipoint N_2-BET isotherm analysis (QuadraSorb, Quantachrome Nova Station A; Table 1).

2.2. Surface charge characterization

2.2.1. Electrophoretic mobility

The electrophoretic mobility (EM) is defined as the response of charged particles that are exposed to an electric field, ultimately yielding charge sign and charge magnitude of particle surfaces. From EM data, zeta potential can be calculated by the Smoluchowski approximation [40], allowing a comparison with the streaming potential measurements detailed below. For the determination of the EM, mineral suspensions with a solid to liquid ratio (SLR) of 0.2 g/L were prepared with varying pH from 3.5–8.0 at a constant ionic strength of 0.1 M NaCl and equilibrated in an overhead rotator (~1 rpm) for 24 h (cf. Exp. I/1–4 in Table S2 in Supporting Information (SI)). The samples were homogenized using an ultra-sound finger immediately before EM measurements using a flow through cell in a Zetasizer Nano MS (Malvern Instruments).

To determine the impact of Ca^{2+} and Al^{3+} ions on the EM additional sets of experiments were conducted at different concentrations of $CaCl_2$ or $AlCl_3$ (5–36 μM) added to a suspension of K-feldspar (cf. Exp. I/5–8 in Table S2 in SI). For characterization of possible precipitates throughout the experiment, mineral suspensions of several samples of K-feldspar with and without 10 μM Al^{3+} as well as An_{99} at three different pH values were investigated by scanning electron microscopy (SEM) and energy dispersive X-ray analysis (EDX). For sample preparation, the mineral suspensions were dried on top of a carbon pad and sputtered with gold. SEM images were captured with an AG-EVO 50 microscope (Carl Zeiss) at a voltage of 15 kV and a working distance of 13 mm. EDX measurements were performed using a Bruker QUANTAX EDS detector to identify possible Al precipitates.

Table 1
Characterization of the used feldspars: composition and specific surface areas. Unless stated otherwise, uncertainties and error bars correspond to a 95% confidence level (2σ) throughout this work. For further details see Table S1 in SI.

	Na: K: Ca	Al: Si	SSA in m^2/g
K-Feldspar (Or)[a]	0.22: 0.78: 0.01	0.26: 0.74	4.2 ± 0.4
Oligoclase (An_{23})	0.72: 0.05: 0.23	0.29: 0.71	2.4 ± 0.4
Labradorite (An_{79})	0.19: 0.02: 0.79	0.21: 0.79	3.9 ± 0.4
Synthetic anorthite (An_{99})	0.01: 0: 0.99	0.50: 0.50	4.1 ± 0.4

[a] Neumann et al. [36]

2.2.2. Streaming potential

Streaming potential experiments were conducted as an alternative approach to characterize the zeta potential of the used mineral powders. The zeta potential corresponds to the electrical potential at the shear plane of a solid/liquid interface. The measured potential includes the charge of the surface, as well as the charge of adsorbed ions within the shear plane.

2.2.2.1. Data acquisition. Streaming potential measurements (cf. Exp. II in Table S2 in SI) were done at room temperature using a SurPass set-up (Anton Paar, Graz, Austria). Anorthite particles of sizes >30 μm were filled into the cylindrical powder cell of the instrument. Solutions of 2 mM $CaCl_2$ or 5 mM NaCl (to yield almost identical ionic strength, I = 5 mM) were prepared. The pH of the initial solution was adjusted to above pH 9 by addition of $Ca(OH)_2$ or NaOH solution, respectively. The solution reservoir was under Argon atmosphere to limit interference from CO_2. Streaming potential was measured first at the initial pH (>9) and continuously while subsequently lowering pH using HCl. Various titration parameters were used to evaluate the influence of rinsing time after titrant addition. At the end of each titration (stop criterion was pH 3) a sample of the solution was kept for ICP-OES (Firma PerkinElmer, 8300DV). The full set of streaming potential and analytical data is shown in Section 5 in the SI.

2.2.2.2. Determination of (de)protonation constants. Streaming potential measurements were used to determine the (de)protonation constants of anorthite by modeling the zeta potential. The zeta potentials were fitted by a combination of UCODE_3.061 [41] as a fitting shell and a modified version of FITEQL2 [42] as an application. The two available streaming potential data sets in 5 mM NaCl were used, with the standard deviations for each data point as weights with UCODE. The slip-plane distance was also fitted, as described in more detail in the results section.

2.3. Sorption experiments

To quantify the sorption of Eu^{3+} and Am^{3+} on plagioclases, batch uptake experiments covering a broad range of geochemical conditions were carried out (see Exp. III in Table S2 in SI for a summary of all data sets). The experimental conditions were similar to our previous work to ensure comparability with the available sorption data for K-feldspar [36].

$EuCl_3 \bullet 6\ H_2O$ (99.99%, abcr GmbH) and a ^{243}Am stock solution (26 μM in 0.01 M HCl) were used to adjust the metal concentration to 0.052–10 μM. The pH value of the mineral suspensions was adjusted to 3–9 by adding small amounts of HCl or NaOH. For batch sorption experiments, mineral suspensions with a SLR of 3 g/L were adjusted to near neutral pH and ionic strengths of 0.01–0.1 M NaCl (Exp. III in Table S2 in SI) before adding appropriate concentrations of the metal ion M^{3+}. Samples were equilibrated in an overhead rotator (~1 rpm) for ~24 h, and the final pH was measured in suspension. Afterwards, liquid and solid phase were separated by centrifugation (20 min, 20,400×*g*) using a Sigma laboratory centrifuge type 3–30KH. All experiments were performed at room temperature under ambient conditions, except for the Am experiments (Exp. III/2,4,6 and 8, cf. Table S2 in SI), which were carried out under inert atmosphere in a nitrogen glovebox for radiation safety reasons. To determine the concentration of Eu^{3+} (as well as Al^{3+}, Ca^{2+}, and Si^{4+} from mineral dissolution), aliquots of the supernatant

were analyzed by ICP-MS (Thermo Fisher Scientific, iCAP RQ, with Sc and Rh as internal standards, 3 replicates). The concentrations of Am^{3+} in the supernatant of the Am samples were examined in duplicates via liquid scintillation counting (LSC), using a HIDEX 300 SL device and the scintillation cocktail Ultima gold.

2.4. Time-resolved laser-induced fluorescence spectroscopy (TRLFS)

For preparation of TRLFS samples, a 10 μM stock solution of ^{248}Cm in 1 M $HClO_4$ was used (Exp. IV in Table S2 in SI). The preparation procedure was analogous to the ^{243}Am samples in the batch sorption experiments (see above, $[Cm^{3+}] = 0.5$ μM, [NaCl] = 0.1 M, SLR = 3 g/L) to ensure comparability. Luminescence of the samples was measured in air atmosphere in quartz cuvettes with a path length of 10 mm. Luminescence was excited using a pulsed Nd:YAG laser (Continuum SureLite SLI-20) coupled with a dye laser system (Radiant NarrowScan K, dye: 1:1 mix of excalite398 and 389 W). A spectrograph (Andor Shamrock SR-303i-A) with a 300 mm^{-1} grating was used as a polychromator with an Andor iStar CCD 334 T for signal detection. Emission spectra were measured for 10 ms after a 1 μs delay relative to the laser pulse. For lifetime measurements the delay between laser pulse and detection was varied in steps of 15–20 μs. All delays were generated by the internal digital delay generator of the camera.

Cm^{3+} strongly absorbs UV light at 396.6 nm, corresponding to the electronic transition $^8S_{7/2} \rightarrow {}^6I_{11/2}$, and typically emits luminescence from its first electronic excited state $^6D_{7/2}$ to the near-degenerate ground state $^8S_{7/2}$. The emission spectrum of the Cm aquo ion shows one broad, asymmetric band at 593.8 nm with a full width half maximum of ~7.7 nm. As a consequence of changes in the first coordination sphere of Cm, e.g., due to surface complexation, the emission band is red shifted (nephelauxetic effect) [43]. Each chemical species exhibits a characteristic band position, which can be obtained by peak deconvolution of the emission spectra. The mathematical ratios between the species obtained from peak deconvolution can be recalculated into a chemical species distribution through fluorescence intensity (FI) factor correction, which takes the reduced quantum yield of excitation and emission due to the red shift into consideration. The Cm aquo ion serves as a reference with a FI factor of 1.0 and mineral surface species typically show reduced values of FI < 1 [20].

The luminescence lifetimes τ can be determined by varying the delay between laser pulse and detection, and fitting the obtained decay curves mono- or bi-exponentially (Section 7.2 in SI). The lifetime τ can be used to determine the amount of water molecules remaining in the first coordination sphere via Kimura's empirical equation [44]:

$$n(H_2O) = 0.65 \times \tau[ms]^{-1} - 0.88.$$

2.5. Thermodynamic sorption modeling and parameter derivation

The surface complexation model could not be developed by straightforward adaptation of the earlier model for K-feldspar [36], due to the different mineral properties (dissolution, surface structure, and deprotonation) within the feldspar group. The dissolution of An_{99} was considered by using its solubility product from Stefánsson and Arnórsson [45] (see Table 2), while the specific site density (SSD) was calculated based on crystallographic data (3.74 sites/nm^2, see Section 2 in SI for details). As described in more detail see Sections 2.2.2 and 3.1.2, the (de)protonation constants log K_a for An_{99} were determined in this study.

Based on the acid base properties of the solid and the aqueous species, the calculation of the formation constants log K of the surface complexes was performed with the geochemical speciation codes PHREEQC (version 3.7.1, [46]) coupled with UCODE_2014 (version 1.004,[47]) using the diffuse double layer (DDL) model by Stumm and Schindler [48–50]. As explained previously, we have chosen the relatively simple but well-established DDL approach: apart from the reasons given in the introduction, this allows straightforward comparison to our previously reported model for K-feldspar [36]. Moreover, practical safety assessment on large scales – as will be required for a nuclear waste disposal site – will have to rely on relatively simple models, in order to keep computational efforts within reasonable constraints and in parallel not requiring the assumption of uniform background electrolytes [51–53]. For the complex solution compositions that are encountered in natural settings, it is currently very difficult to account for the interaction of these components with surfaces in more advanced models. The ThermoChimie (10a, Version of September 26, 2018) thermodynamic database was chosen for the modeling. Adsorption of negatively charged carbonate species on feldspar was not considered, as it was shown not to occur in similar systems such as K-feldspar [36] and quartz [54].

Based on the aqueous speciation and the protolysis model, the An_{99} adsorption model was designed. This is described in more details in the results section. The same combination of shell fitting codes as described for the above approach was used. All experimental observations related to M^{3+} adsorption were treated with the weighing factor set to 1. Therefore, the (very small) error for the fitted equilibrium constants obtained from UCODE is not used, and instead set to ± 0.5 to be in a realistic range.

Table 2
Formation equations and corresponding log K values for relevant aqueous species and solids of Eu as representative for lanthanides and the trivalent actinides Am and Cm in the generic modeling approach, anorthite (An_{99}) dissolution and surface (de)protonations.

Species	log K
$M^{3+} + Cl^- = MCl^{2+}$	0.76[a]
$M^{3+} + 2Cl^- = MCl_2^+$	−0.05[a]
$M^{3+} + H_2O - H^+ = M(OH)^{2+}$	-7.80[a]
$M^{3+} + 2\ H_2O - 2\ H^+ = M(OH)_2^+$	-15.70[a]
$M^{3+} + 3\ H_2O - 3\ H^+ = M(OH)_3(aq)$	-26.20[a]
$M^{3+} + 4\ H_2O - 4\ H^+ = M(OH)_4^-$	-40.70[a]
$M^{3+} + HCO_3^- = M(HCO_3)^{2+}$	12.43[a]
$M^{3+} + CO_3^{2-} = M(CO_3)^+$	7.90[a]
$M^{3+} + 2CO_3^{2-} = M(CO_3)_2^-$	12.90[a]
$M^{3+} + 3CO_3^{2-} = M(CO_3)_3^{3-}$	14.8[a]
$M^{3+} + H_4(SiO_4) - H^+ = MSiO(OH)_3^{2+}$	−2.62[a]
$M^{3+} + Ca^{2+} + 3\ H_2O - 3\ H^+ = CaM(OH)_3^{2+}$	−26.3[a]
$M^{3+} + 2Ca^{2+} + 4\ H_2O - 4\ H^+ = Ca_2M(OH)_4^{3+}$	−37.2[a]
$M^{3+} + 3Ca^{2+} + 6\ H_2O - 6\ H^+ = Ca_3M(OH)_6^{3+}$	−60.7[a]
$M(OH)_3(am) = M^{3+} + 3\ H_2O - 3\ H^+$	17.60[a]
$MCO_3OH(cr) = M^{3+} + H_2O + CO_3^{2-} - H^+$	-9.63[a]
$MCO_3OH{\cdot}0.5\ H_2O(s) = M^{3+} + 1.5\ H_2O + CO_3^{2-} - H^+$	-7.80[a]
$CaAl_2Si_2O_8 = Ca^{2+} + 2Al(OH)_4 + 2\ H_4SiO_4(aq) - 8\ H_2O$	-24.15[b]
$\equiv(S\text{-}OH) + H^+ = \equiv(S\text{-}OH_2)^+$	+6.84 ± 0.38[c]
$\equiv(S\text{-}OH) - H^+ = \equiv(S\text{-}O)^-$	−6.94 ± 0.38[c]

[a] ThermoChimie-TDB (10a Version of September 26, 2018), [b] Stefánsson and Arnórsson [45], [c] This work, based on experimental error estimates, as explained in the text.

3. Results and discussion

3.1. Surface charge characterization

3.1.1. Electrophoretic mobility of different feldspars

Differences in cation composition and Al:Si ratio between K- and Ca-feldspars are expected to result in changes in the surface charge of the two mineral groups. To test this hypothesis, the EM for Ab, An_{99}, and plagioclases with different Ca amounts was measured and compared to data previously published for K-feldspar [36] (Fig. 1**a**). All investigated feldspars show similar surface properties at low pH, i.e., their isoelectric point is at pH < 2, and a decrease of the EM for all feldspars is observed for pH = 2–4, indicating an increased negative charge of the mineral particles due to surface site deprotonation with increasing pH. No significant differences between the Ab and K-feldspar data are observed over the entire investigated pH range, suggesting a similar surface charge behavior, i.e., isoelectric point and site (de)protonation constants, for alkali feldspars.

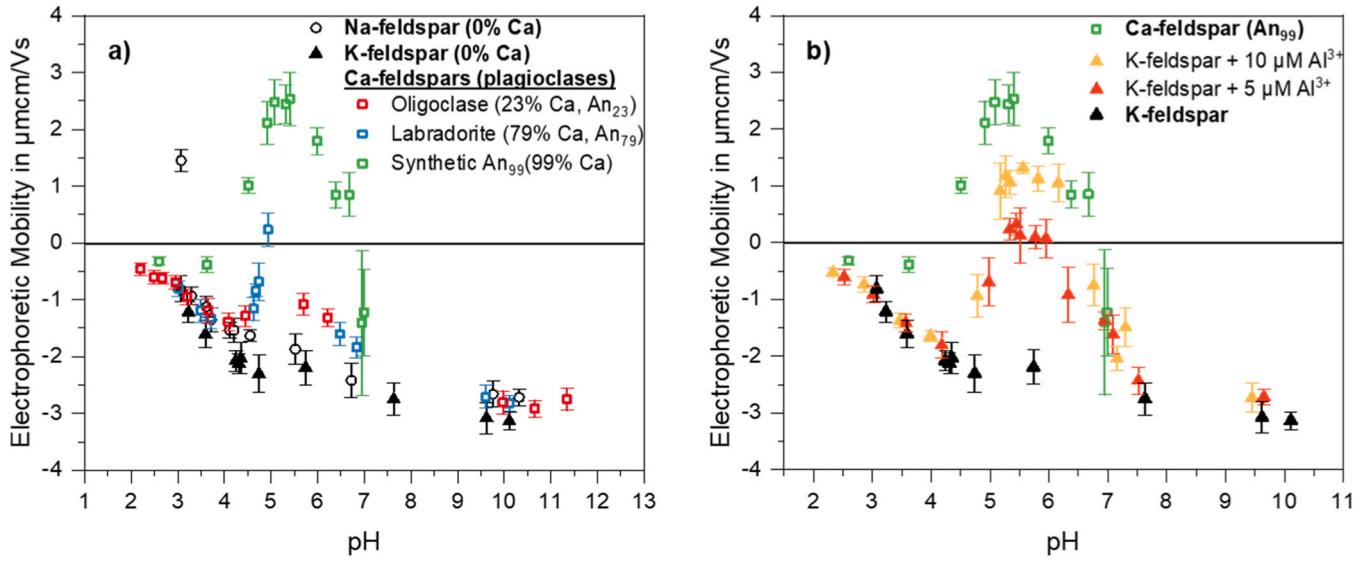

Fig. 1. EM data of a) Ab (empty circles) and plagioclases ($An_{23,\ 79,\ 99}$; colored squares) with different Ca amounts, measured at SLR = 0.2 g/L feldspar in 0.1 M NaCl, and comparison to K-feldspar data under identical experimental conditions from literature (black triangles) [36], b) EM data of K-feldspar with different amounts of added Al^{3+}.

In contrast to the previously reported trend for K-feldspar, the EM of the investigated plagioclases increases for pH = 4–5.5, with a strong correlation to the increase in Ca^{2+} content in the crystal lattice. In the case of An_{79} and An_{99}, the sign of EM is even reversed and becomes positive for pH 4–7 (Fig. 1**a**). This charge reversal is likely connected to stronger dissolution of the plagioclases in comparison to the alkali feldspars with increasing amount of Ca and Al in the crystal lattice [55, 56] (see Figure S2 in SI). In consequence, the concentration of Ca^{2+} and Al^{3+} in solution is higher for plagioclases than for alkali feldspars and they can re-adsorb on the mineral surface, compensating the negative surface charge and consequently raise the EM. Interestingly, the adsorption of Ca^{2+} and Al^{3+} overcompensates the bare surface charge, leading to a charge reversal. Similar effects have been described previously for the adsorption of Al^{3+} on sapphire-c and clay minerals [57]. For pH > 5.5, an abrupt decrease of the EM is observed for the plagioclases, resulting in comparable values for all investigated feldspars for pH > 7.5 (discussed below).

To test the impact of adsorbed Ca^{2+} and Al^{3+} on the EM, small amounts of Ca^{2+} (25–36 µM) or Al^{3+} (5–10 µM, concentration ranges chosen based on dissolution data of anorthite) were added to a suspension of K-feldspar. Addition of Ca^{2+} leads to a small increase of the EM in the pH range 4–7 (Figure S4 in SI) but does not cause a reversal of the mineral's surface charge. The addition of small amounts of Al^{3+} leads to a much stronger increase and sign reversal of the EM (Fig. 1**b**), comparable to what was observed for the plagioclases. Likely, both Ca^{2+} and Al^{3+} contribute to the observed surface charge effect, with Al^{3+} having a more pronounced impact.

The mechanism behind the surface charge reversal can be Al^{3+} adsorption, the precipitation of an Al secondary solid phase at the interface, or a combination of both processes. Precipitation seems plausible, when taking the solubility minimum of amorphous $Al(OH)_3$ at pH ~ 6 into account (see dashed line in Figure S3 in SI). Moreover, the increase in solubility of Al^{3+} at pH > 6 coincides with the strong decrease in EM, as observed in Fig. 1. We detect Al^{3+} concentrations of 7–90 µM in the supernatant of our samples, which would lead to the precipitation of a maximum of 460 µg $Al(OH)_3$ if all the Al^{3+} in the aqueous phase precipitated completely. However, PXRD and SEM investigations did not prove the existence of such a phase, possibly due to the very low quantity combined with a low degree of crystallinity (see Section 4 in SI). The results presented here are consistent with a study by Lützenkirchen et al., who described a similar charge reversal for the adsorption/precipitation of Al^{3+} on kaolinite and sapphire [57]. Similarly, the epitaxial growth of monolayer gibbsite on the muscovite basal plane [58] has been reported. Despite higher [Al^{3+}] (1 mM) and lower pH (4.15), similar mechanisms may occur for feldspars under the investigated experimental conditions [59].

3.1.2. *Determination of protonation constants of anorthite from zeta potential*

(De)protonation constants of An_{99} and a slip plane distance were determined by modeling zeta potential data from streaming potential measurements. The shape of the curve is in good agreement with the EM measurements described above and in particular the same isoelectric point (IEP) at pH 6.8 is obtained.

For modeling the zeta potential, the slip plane distance is needed. Hiemstra et al. quantified the location at the slip plane within the gibbsite interface in order to describe electrokinetic data [60]. Dzombak and Morel suggested to use a variable location of the slip plane in the DDL depending on the ionic strength [30] and suggest that the distance between the slip plane and the head end of the DDL is proportional to the square root of the ionic strength of the equilibrium solution (see Fig. 2**b**), corresponding to the Gouy-Chapman model [60]. For our system of An_{99} in 5 mM NaCl, a slip plane distance of 3 nm was calculated and applied for the fitting of the zeta potential data and the IEP. This result is in very good agreement with the work of Hiemstra et al.

Modeling the zeta potential. To obtain (de)protonation constants from the streaming potential measurements (Figure 2)we chose a similar approach to that of Dzombak and Morel for TiO_2 [30]. The specific conditions for the experiments are given in the SI (section 5.1.2). To be consistent with previous modeling work within the same project, a DDL model was chosen including two (de)protonation constants. The protonation deprotonation reactions considered were

$$\equiv S-OH+H^{+}\rightleftharpoons\equiv S-OH_2^{+};K^{+} \quad (1)$$

$$\equiv S-OH\rightleftharpoons\equiv S-O^{-}+H^{+};K^{-} \quad (2)$$

Using a modified version of FITEQL that includes slip plane distance coupled to UCODE yielded the following parameters: log $K^{+} = +6.84 \pm 0.38$, log $K^{-} = -6.94 \pm 0.38$, $x_z = 0.72 \pm 0.03$. The parameter x_z corresponds to the slip plane distance relative to the Debye length. The fitting was done on two duplicate series of experiments, for which the obtained experimental errors (standard deviations from six

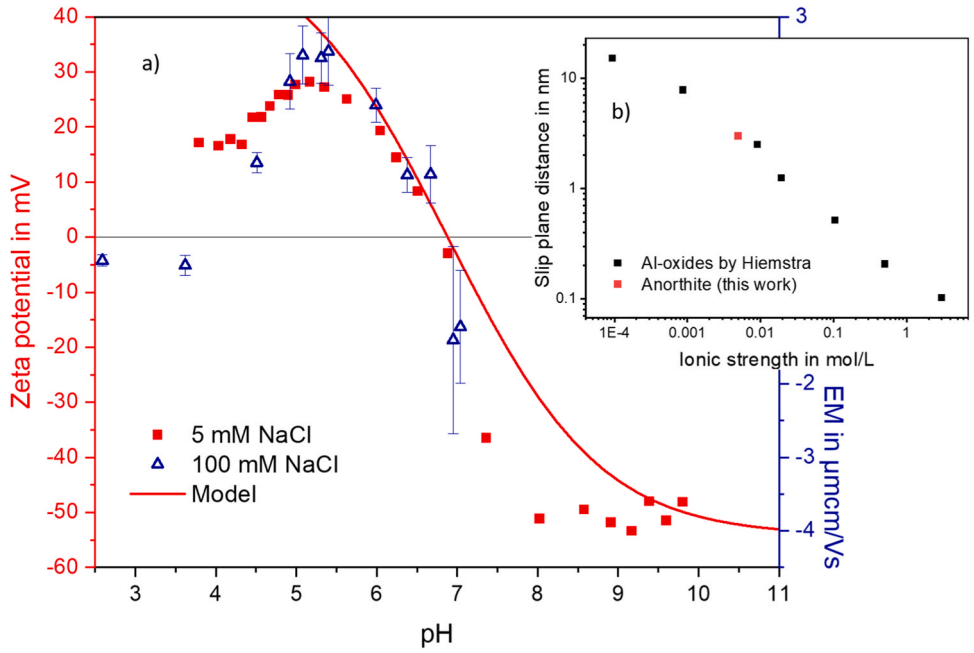

Fig. 2. a) Streaming potential data (red) at 5 mM NaCl solutions for An_{99} in comparison to EM data (blue) at 100 mM NaCl, as well as model (solid line) based on the log K_a values given in the text. b) Empirical relation between the ionic strength and the slip plane distance (i. e., apparent location of the plane of shear) for gibbsite and an aluminum oxide by Hiemstra et al. [60] in black. Red indicates our value for the studied An_{99}.

measurements per pH) were applied to the UCODE fitting.

We consider the values for log K to be reliable because the slip plane distance follows the expected behavior (Fig. 2**b**) and the slope of the zeta potential around the isoelectric point is very steep.

Interestingly, the observed (de)protonation constants of An_{99} are several magnitudes higher than the previous obtained log K_a value for K-feldspar (log $K_a = -2.5 \pm 0.02$ [36]). Despite the similarities in crystal structures of the two feldspars, the surface chemistry at the mineral-water interface differs significantly, as observed also by EM measurements. Several explanations are possible for this observation, which are not mutually exclusive. It is known that silanol surface groups are more acidic than aluminol groups [61,62]. Consequently, the higher Al:Si ratio in An_{99} should shift the protonation constant towards higher values. In addition, our EM measurements suggest adsorption or precipitation of Al^{3+} on the surface at near-neutral pH values, which may lead to yet more "Al-O"-type groups to be exposed on the surface. To elucidate and potentially disentangle these processes, further investigations focusing on the impact of Al^{3+} on the feldspar surface chemistry on a molecular level will be necessary.

3.2. Batch sorption experiments

Quantitative analysis of M^{3+} sorption onto the different plagioclases was carried out via an extensive set of batch sorption experiments (see Table S2 Exp. III in SI for overview). For the subsequent discussion, two different geochemical conditions were chosen exemplarily – low [M^{3+}] ([$^{243}Am^{3+}$] = 52 nM) and high [M^{3+}] ([Eu^{3+}] = 10 µM). The results, shown in Fig. 3, are also compared to the data available for K-feldspar

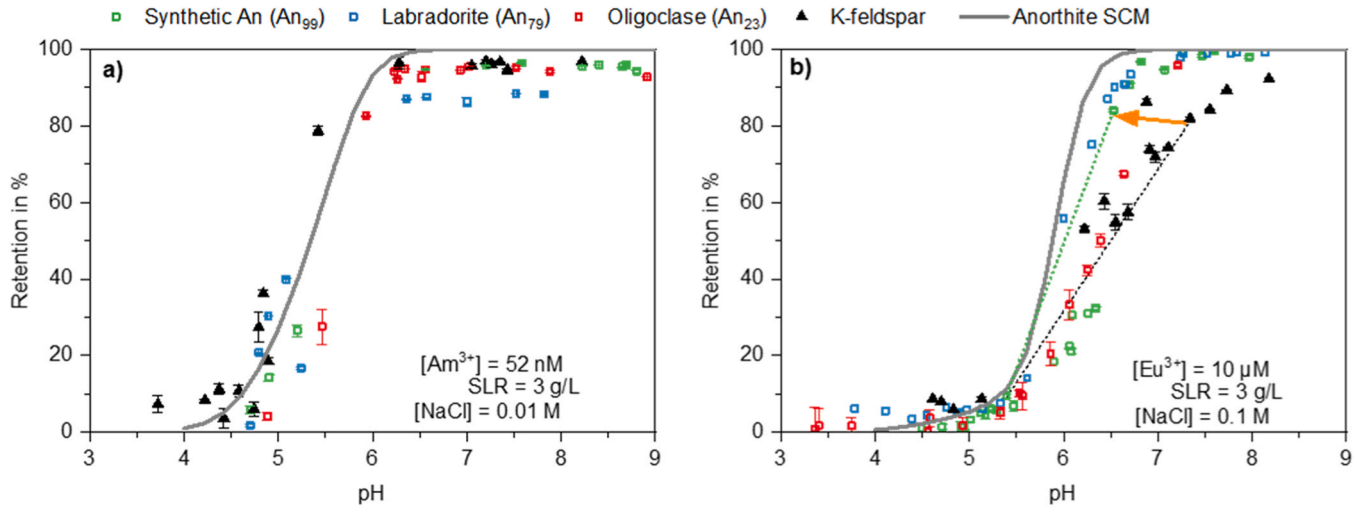

Fig. 3. Batch sorption data of two selected geochemical conditions. The solid, gray lines show the calculated retention of M^{3+} by An_{99} based on the developed SCM (see Section 3.4.). **a)** Low [M^{3+}] ([$^{243}Am^{3+}$] = 52 nM), **b)** high [M^{3+}] ([Eu^{3+}] = 10 µM) with dashed lines as a guide-to-the-eye to indicate differences in the slopes of the sorption edges for An_{99} (green) and K-feldspar (black). The orange arrow indicating the difference of the slope. Data for K-feldspar are taken from our previous work [36].

under identical experimental conditions [36]. Generally, sorption is weak for pH < 4 for all plagioclases in all investigated series. Based on the determined electrophoretic data, the uptake coincides with the change in the trend of the surface charging curve. With increasing pH, retention of the trivalent metal ions increases. The slope of the sorption edge at low [M^{3+}] at pH ~ 5 is extremely steep, while at high [M^{3+}] the edge is slightly flattened for all plagioclases. Uptake of metal ions is quantitative for pH > 6.5.

For low [M^{3+}] the data for all plagioclases and anorthite fall on the same line, however, the plagioclases show differences in uptake at high [M^{3+}]. Sorption of M^{3+} on all feldspars at high metal concentrations starts at pH 5. For pH > 5, the slope of the sorption edge increases with increasing Ca^{2+} content in the crystal lattice of the mineral.

When comparing electrophoretic data and the position of the sorption edge of trivalent metal ions on An_{99} (see Figure S12 in Section 6 of SI), it is striking that the strong increase of sorption of M^{3+} occurs in the same pH range where the strong decrease of EM is observed, i.e., pH ~ 6. The strong decrease of EM and the strong increase of the sorption on the plagioclases appear to be related to each other. The exact reasons, however, may involve more than mere electrostatics. Once again, multiple molecular processes may be responsible for the observed macroscopic effect. Anorthite has a slightly higher number of sorption sites (3.74 sites/nm^2) than K-feldspar (3.30 sites/nm^2). A sufficient number of binding sites for complete uptake is accessible . As mentioned above, An_{99} will exhibit more aluminol instead of silanol sites than Or, which are more reactive, albeit determined for pure Al and Si oxides [61,62]. Additionally, the stronger dissolution of plagioclases leads to a higher surface roughness, causing a slightly larger surface area available for sorption [55]. Our data does not allow to conclusively decide which of these processes is most relevant for the observed behavior. Nonetheless, our data show clearly how seemingly small differences in mineralogy – such as between K- and Ca-feldspars – may cause significant differences in the mineral's retention capacity.

3.3. TRLFS – Sorption speciation on synthetic anorthite

3.3.1. Emission spectra and peak deconvolution

Our surface charge experiments have revealed differences in the surface characteristics of feldspars, depending on their Ca content and our sorption experiments have established that these different surface properties affect the retention of trivalent lanthanides and actinides. To identify reasons for this effect on heavy metal retention, TRLFS was applied to determine the interfacial speciation on the molecular scale. Cm^{3+} was used as a luminescence probe to identify the complexes formed on the surface of anorthite. The measured emission spectra are displayed in Fig. 4. A strong red shift with increasing pH (> 5) is observed, indicative of increasing surface complexation, i.e., IS adsorption. This is consistent with the onset of sorption at a similar pH in the batch sorption experiments. Peak deconvolution of the emission spectra typically delivers single component spectra of the formed surface complexes. Here, however, common peak deconvolution approaches failed due to the simultaneous formation of at least two species. Emission spectra up to pH 4.99 are identical to the Cm aquo ion's, while the spectrum at the subsequent pH (5.24) consists of the Cm aquo ion and two surface complexes (see Figure S13 in SI). Therefore, peak deconvolution using the known single component spectra of Cm adsorbed on K-feldspar [36] was tested and resulted in low residuals (see black lines in Fig. 4), indicating the suitability of the approach. This result is surprising given significant differences in the background fluorescence signals from transition metal impurities in the previous measurements for natural K-feldspar [36]. We conclude that the Cm species on the surfaces of An_{99} and K-feldspars are so similar in their first coordination sphere that they cannot be distinguished spectroscopically. Similar observations were made for sorption on Al and Si oxides [34,63], for which peak positions of surface complexes are generally found to be very similar. More specifically, we find three surface complexes with band

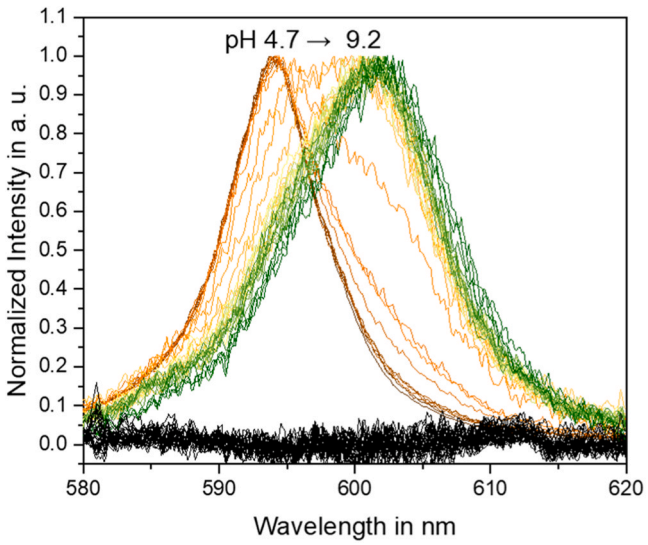

Fig. 4. Emission spectra of synthetic anorthite (SLR = 3 g/L) suspension samples at 0.5 μM Cm^{3+} and 0.1 M NaCl at various pH values (orange to green color pattern). Residuals from spectra deconvolution are plotted as black lines. Spectra are scaled to have the same peak maximum.

positions of 598.5 (Species 2), 602.7 (Species 3), and 605.6 nm (Species 4), which for K-feldspar were assigned as an IS complex ($(\equiv S\text{-}O)_2Cm^+$) and its two hydrolysis forms, $(\equiv S\text{-}O)_2Cm(OH)$ and $(\equiv S\text{-}O)_2Cm(OH)_2^-$ [36]. These band positions are almost identical with Cm adsorbed on bayerite and corundum, i. e., 600.7, 603.0, and 605.4 nm. [24].

3.3.2. Luminescence lifetimes

To validate the assignment of the sorption species, emission lifetimes of Cm on the synthetic An_{99} were measured. The use of a synthetic feldspar avoids additional luminescence signals by rare earth impurities or quenching effects by transition metals (e.g. Fe or Mn [64]) that are commonly present in natural minerals, and which had interfered in our previous study on natural K-feldspar, where luminescence lifetimes could not be analyzed [36]. In the present system, the determination of lifetimes for each species was complicated by their co-occurrence, but an analysis is nonetheless possible.

In general, emission lifetimes were found to increase with increasing pH. This observation is consistent with the formation of IS complexes, which lose water molecules from their first coordination sphere. The emission decay curves were fitted bi-exponentially (see Section 7.2 in SI) to yield the emission lifetimes of the surface complexes (see Table S5 in SI). One species is the Cm aquo ion with its typical lifetime of 68 μs, whereas the surface complexes possess emission lifetimes of 140–150 μs. The calculation of the number of remaining water molecules in the Cm hydration shell using Kimura's equation [44] results in four water molecules for the surface complexes. Since the replacement of H_2O by OH^- has no impact on the emission lifetime [63] and the emission lifetimes of the three identified surface complexes are identical within error, the lifetime study corroborates the assignment as an IS complex and its hydrolysis species, confirming the species assignment made for K-feldspar [36]. For pH > 10, an additional lifetime of ~ 400 μs is observed, corresponding to only 2.5 H_2O in the first coordination sphere, which indicates a higher number of water molecules have been replaced. This can be interpreted as either "surface incorporation" [65] or a ternary complex with an additional ligand from the solution [63,65,66], which would be spectroscopically identical. In either case, this species is only a minor contribution to the overall Cm speciation, and will be irrelevant under typical geochemical conditions.

3.3.3. Quantitative species distribution

From peak deconvolution of the Cm emission spectra (Fig. 4), the

quantitative species distribution can be obtained as a function of pH after FI factor correction [20]. Since peak deconvolution of the emission spectra was conducted using the single component spectra of the previously published K-feldspar [36], the corresponding FI factors were used as well (Species 1 (aquo ion): 1, Species 2: 0.5, Species 3: 0.27, Species 4: 0.18). These values were determined using an empirical equation for calculation of FI factors for sorption species of Cm^{3+} on various minerals [20]. It should be noted that the uncertainties of these FI factors are relatively large due to the applied approximations, i.e., the experimentally derived values of other minerals in Eibl et al. scatter by up to ±0.2 and become larger with increasing red shift of the single component spectrum of the respective species, because of the decreasing luminescence intensity. The obtained corrected species distribution for Cm sorption on An_{99} is displayed in Fig. 5. The contribution of the Cm aquo ion (black) decreases for pH > 5 due the formation of IS complexes. No aquo ion is detected for pH > 6, i.e. at a slightly lower pH compared to K-feldspar. The non-hydrolyzed IS Species 2 which is bound to a protonated surface (red) starts to form at pH 5 and reaches a contribution of ~20% between pH 6–7. The amount of this species is smaller for An_{99} compared to K-feldspar, for which it reaches almost 40% at the same pH. The reason becomes clear when analyzing the contribution of the IS species which is bound to a deprotonated surface (Species 3, blue). As described above, this species forms at much lower pH than on K-feldspar, leading to its co-occurrence with Species 2. Its contribution exhibits a steep increase up to pH 6, where it reaches ~70% relative abundance, corresponding to a higher contribution compared to the K-feldspar (60%). Species 4 is observed from pH > 7 with no major differences in the quantitative amounts among the Ca- and K-feldspars.

Overall, the TRLFS investigations show that spectroscopically identical surface complexes form on Ca- and K-feldspar, whereas, the IS species hydrolyzes at much lower pH in the case of the Ca-feldspar. This coincides with the steeper sorption edge in the same pH range, suggesting a connection between the two observations.

3.4. Surface complexation modeling for Ca-feldspars

Based on batch sorption data, an SCM was developed to quantify the sorption of trivalent actinides on the mineral surface on An_{99} at different geochemical conditions. Due to the uncertainty in the speciation derived from TRLFS and because of the simultaneous appearance of Species 2 and 3, the data were only used to guide the fit with respect to the number of species present in the system. Thus, the SCM considers three IS complexes. The OS species that was used to describe sorption at low pH for K-feldspar [36] was not necessary to reproduce the data of the An_{99}.

The SCM yields the formation constants (log K) of the surface complexes formed on An_{99}: −0.7 ± 1.0, −7.4 ± 1.0, and −12.5 ± 1.0 for Species 2, 3, and 4, respectively (see Table 3). The values are identical within errors to those of K-feldspar, except for the log K of Species 4 (the second hydrolyzed surface species). Here, the SCM identifies a different chemical species than TRLFS and previously on K-feldspar. Due to the different protonation behavior of An_{99}, Species 2 is not a hydrolysis form of the IS, but rather unhydrolyzed Cm bound to a protonated surface site. It should be mentioned here, that TRLFS may not be sensitive to the placement of the proton at the surface, which makes the deconvolution impossible.

The performance of the SCM to reproduce batch sorption data is displayed as lines for low and high $[M^{3+}]$ in Fig. 3. The model describes the data reasonably well at low $[M^{3+}]$, but slightly overestimates retention at higher metal concentration. The agreement with the quantitative data is generally favorable and, most importantly, the model is capable of reproducing the shift to a steeper pH edge with higher Ca content satisfactorily.

The quantitative contributions of the surface species on An_{99} predicted by the model can be compared with the experimental species distribution obtained by TRLFS (lines in Fig. 5). Here, major disagreements become apparent. Species 1, the contribution of the Cm aquo ion (black), is well reproduced, but starts at slightly lower pH in the experimental data compared to the model prediction. This may be caused by a small amount of OS sorption that cannot be distinguished spectroscopically from the Cm aquo ion, since no changes in the first hydration shell occur. No OS species is considered in the SCM, which may cause this discrepancy. More significant differences are found for the adsorbed Species 2–4. The SCM overestimates the formation of

Table 3
Formation equations of spectroscopically identified surface complexes and their corresponding complex formation constants (log K) for Ca- and K-feldspar. Uncertainties correspond to a 95% confidence level (2σ). The numbering follows the TRLFS assignment, where species 1 is the Cm aquo ion. M^{3+} represents Am^{3+}, Cm^{3+}, and Eu^{3+} in the applied generic modeling approach.

Ca-feldspar[a] Species	K-feldspar[b] Species	Surface complex formation	Ca-feldspar[a] log K	K-feldspar[b] log K
2	N/A	$2 \equiv$ S-OH + M^{3+} - $H^+ \rightleftharpoons$ ($\equiv$S-O)($\equiv$S-OH)M^{2+}	−0.7 ± 1.0	-
3	2	$2 \equiv$ S-OH + M^{3+} − 2 $H^+ \rightleftharpoons$ ($\equiv$S-O)$_2M^+$	-7.4 ± 1.0	−8.0 ± 0.9
4	3	$2 \equiv$ S-OH + M^{3+} + H_2O − 3 $H^+ \rightleftharpoons$ ($\equiv$S-O)$_2$M(OH)	-12.5 ± 1.0	−11.6 ± 0.2
N/A	4	$2 \equiv$ S-OH + M^{3+} + 2 H_2O − 4 $H^+ \rightleftharpoons$ ($\equiv$S-O)$_2$M(OH)$_2$	-	−16.6 ± 0.4

[a] This study, [b] Neumann et al. [36].

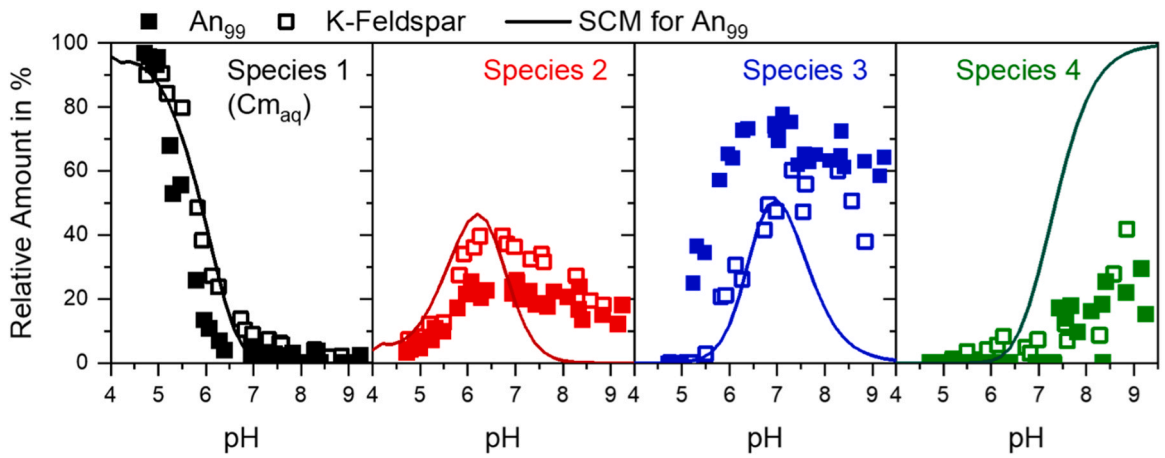

Fig. 5. FI-corrected quantitative species distribution of sorption of 0.5 µM Cm^{3+} adsorbed on 3 g/L syn. An_{99} (filled symbols) at 0.1 M NaCl and comparison to previously published data of K-feldspar (empty symbols, [36]) and via SCM calculated species distribution (lines) under identical experimental conditions.

Species 2 by about a factor of two (max. abundance 45% instead of 20%), while underestimating the formation of Species 3 by about the same factor (max. abundance. 50% instead of 75%). This may be related to the issues with the simultaneous appearance of these two species in our experimental work. Above pH ~7, the model predicts a decline of the relative abundance of Species 3, which was not observed experimentally. This is caused by the relative abundance of Species 4, which constitutes the largest inconsistency between experiment and model. Species 4 appears at a too low pH of ~6, and its contribution is greatly overestimated by the SCM for all pH values >6. It is unclear why this substantial discrepancy occurs, but despite a multitude of attempts, no model could be derived that was capable of describing the quantitative retention and the relative abundance of the experimentally verified species. It is likely, that the surface chemistry connected to the charge reversal caused by Al^{3+} adsorption and/or precipitation, is currently not sufficiently understood to derive a consistent set of surface (de-)protonation and surface complexation constants for M^{3+} on An_{99}. In this respect, significantly more work is required to identify the interfacial reactions controlling the interaction of Al^{3+} with the mineral surface. Beyond uptake quantification, which is complicated by the fact that the mineral is both source and sink for Al^{3+}, this will require a correct identification of the uptake mechanism(s), for instance IS and OS adsorption or precipitation in solution or at the mineral surface. Only when both, mechanism(s) and quantification of Al^{3+} uptake on feldspars, are available from experimental data, a comprehensive SCM for the reaction can be developed, which will then provide a more accurate thermodynamic description for M^{3+} adsorption investigated in this work.

4. Conclusions

We have studied the surface chemistry of synthetic anorthite and natural plagioclases and the adsorption of trivalent actinides and lanthanides on these minerals. As a first step, all minerals were characterized by EM (and anorthite in addition by streaming potential measurements), with the aim to characterize their surface charge and acid base properties. The data consistently show that the charge of the particles does not follow the simple continuously decreasing trend seen for K-feldspar, but instead increases from pH 4–5.5, after which it decreases rapidly to again match the K-feldspar behavior from pH ~7.5. Experiments with K-feldspar in the presence of Al^{3+} show that this behavior is related to an interfacial reaction – most likely adsorption and/or surface precipitation – involving Al^{3+}. The return to negative surface charges indicates a dissolution of the surface precipitate or desorption of Al^{3+}. Ca^{2+} induces a similar, but much less pronounced, effect. This indicates a complex interplay between dissolution of the mineral, producing dissolved Ca^{2+} and Al^{3+}, and re-adsorption and/or precipitation, which affects all subsequent processes. The (de)protonation constants of anorthite were determined from zeta potential modeling to be

$\log K^{+} = +6.84 \pm 0.38$ (for the surface reaction: $\equiv S - OH + H^{+} \leftrightarrow \equiv S - OH_2^{+}$) and

$\log K^{-} = -6.94 \pm 0.38$ (for the surface reaction: $\equiv S - OH \leftrightarrow \equiv S - O^{-} + H^{+}$).

Firstly, these surface processes can be identified in sorption edges for M(III) which exhibit a systematic increase in their slope depending on the mineral's Ca and Al content. The steep increase in sorption coincides with the desorption/re-dissolution of Al^{3+}, which creates sorption sites for other metals (here, Cm^{3+}), but necessitates a stronger variation in the surface charge. The same process also affects the speciation of M^{3+} on the mineral surface. TRLFS indicates that the species formed in the sorption process are spectroscopically indistinguishable from those previously reported for K-feldspar, but their relative abundance is different. The biggest difference is seen in the earlier formation and greater abundance of the singly hydrolyzed IS complex (Species 3) at lower pH (~5) than on K-feldspar. This stronger hydrolysis coinciding with the steep increase in retention at these pH values.

In addition, a DDL surface complexation model was developed based on the sorption edges of An_{99}. From this model, formation constants for the three surface complexes can be derived as $\log K_1 = -0.7 \pm 1.0$, $\log K_2 = -7.4 \pm 1.0$, and $\log K_3 = -12.5 \pm 1.0$. These constants are capable of reproducing the sorption edges at high and low $[M^{3+}]$. Unfortunately, the current model does not fully agree with the experimental data in the assigned chemical species and fails to reproduce their relative abundance over wide pH ranges.

In summary, our study shows that Ca-bearing feldspars strongly immobilize trivalent heavy metals, even stronger than alkali feldspars, especially at high $[M^{3+}]$. The complex surface chemistry of anorthite and dynamic surface reactivity, due to the relatively high solubility of the mineral, however, complicate the accurate chemical and quantitative description of the relevant processes. In particular, the molecular level interactions of feldspar surfaces with Al^{3+}, and subsequently the impact of these reactions on the retention of other cations needs to be the focus of future investigations. These findings are highly relevant for the risk assessment of nuclear waste disposal sites in crystalline bedrock, as well as other processes where the transport of heavy metal contaminants in the geosphere is of importance, such as clean-up efforts in contaminated sites, mining of uranium and rare earths, or accidental release scenarios.

Funding

This work was supported by the German Federal Ministry of Economics and Technology (BMWi) through the SMILE project with grants 02E 11668 A and 02E 11668 C and the German Federal Ministry for the Environment, Nature Conservation, Nuclear Safety and Consumer Protection (BMUV) via the KURSIV project with grants 02E 12052 A and 02E 12052 C.

Declaration of Competing Interest

The authors declare that they have no known competing financial interests or personal relationships that could have appeared to influence the work reported in this paper.

Data availability

Data will be made available on request.

Acknowledgments

The authors thank the Mineraliensammlung of the TU Bergakademie Freiberg for providing the labradorite mineral samples, Dr. Robert Möckel of Helmholtz Institute Freiberg for Resource Technology for performing XFA analysis, Sabrina Beutner for ICP-MS measurements as well as Salim Shams Aldin Azzam for PXRD measurements.

Appendix A. Supporting information

Supplementary data associated with this article can be found in the online version at doi:10.1016/j.colsurfa.2024.133529.

References

[1] Payne T., Davis J., Ochs M., Olin M., Tweed C., NEA Sorption Project Phase II: Interpretation and Prediction of Radionuclide Sorption onto Substrates Relevant for Radioactive Waste Disposal Using Thermodynamic Sorption Models, OECD NEA Nuclear Energy Agency, Paris, 2006.

[2] S. Briggs, J. McKelvie, B. Sleep, M. Krol, Multi-dimensional transport modelling of corrosive agents through a bentonite buffer in a Canadian deep geological repository, Sci. Total Environ. 599–600 (2017) 348–354, https://doi.org/10.1016/j.scitotenv.2017.04.242.

[3] H. Geckeis, J. Lützenkirchen, R. Polly, T. Rabung, M. Schmidt, Mineral-water interface reactions of actinides, Chem. Rev. 113 (2013) 1016–1062, https://doi.org/10.1021/cr300370h.

[4] B.G.R. (Bundesanstalt für Geowissenschaften und Rohstoffe), Endlagerung radioaktiver Abfälle in Deutschland - Untersuchung und Bewertung von Regionen mit potenziell geeigneten Wirtsgesteinsformationen, Hannover/Berlin, 2007.

[5] S. Pettersson, B. Loennerberg, Final repository for spent nuclear fuel in granite-the KBS-3V concept in Sweden and Finland, SKB (Swedish Nuclear Fuel and Waste Management Company), Prague, 2008.

[6] A. Ström, J. Andersson, K. Skagius, A. Winberg, Site descriptive modelling during characterization for a geological repository for nuclear waste in Sweden, Appl. Geochem. 23 (2008) 1747–1760, https://doi.org/10.1016/j.apgeochem.2008.02.014.

[7] J. Andersson, K. Skagius, A. Winberg, T. Lindborg, A. Ström, Site-descriptive modelling for a final repository for spent nuclear fuel in Sweden, Environ. Earth Sci. 69 (2013) 1045–1060, https://doi.org/10.1007/s12665-013-2226-1.

[8] P.E. Mariner, E.R. Stein, E.A. Kalinina, T. Hadgu, C.F. Jove-Colon, E. Basurto, 2018, US Sections Prepared for Future NEA Crystalline Club (CRC) Report on Status of R&D in CRC Countries Investigating Deep Geologic Disposal in Crystalline Rock. pp. 1–47..

[9] N.P. Laverov, S.V. Yudintsev, B.T. Kochkin, V.I. Malkovsky, The Russian strategy of using crystalline rock as a repository for nuclear waste, Elements 12 (2016) 253–256, https://doi.org/10.2113/gselements.12.4.253.

[10] J. Wang, High-level radioactive waste disposal in China: update 2010, J. Rock. Mech. Geotech. Eng. 2 (2010) 1–11, https://doi.org/10.3724/SP.J.1235.2010.00001.

[11] A. Vokál, D. Vopálka, P. Vecerník, An approach for acquiring data for description of diffusion in safety assessment of radioactive waste repositories, J. Radioanal. Nucl. Chem. 286 (2010) 751–757, https://doi.org/10.1007/s10967-010-0763-6.

[12] K. Yamamoto, H. Yoshida, F. Akagawa, S. Nishimoto, R. Metcalfe, Redox front Penetration in the Fractured Toki Granite, central Japan: An Analogue for Redox Reactions and Redox Buffering in Fractured Crystalline Host Rocks for Repositories of Long-lived Radioactive Waste, Elsevier Ltd, 2013, 10.1016/j.apgeochem.2013.03.013.

[13] M. Okrusch, S. Matthes, Mineralogie, Springer Berlin Heidelberg,, Berlin, Heidelberg, 2014, https://doi.org/10.1007/978-3-642-34660-6.

[14] R.D. Shannon, Revised effective ionic radii and systematic studies of interatomic distances in halides and chalcogenides, Acta Crystallogr. Sect. A. 32 (1976) 751–767, https://doi.org/10.1107/S0567739476001551.

[15] J.V. Smith, W.L. Brown, Feldspar Minerals 1 Crystal Structure and Physical Properties, Springer,, Berlin, 1974, https://doi.org/10.1007/978-3-642-96173-1.

[16] K. Gompper, Zur Abtrennung langlebiger Radionuklide; FZKA, Karlsruhe, 2001.

[17] D.L. Clark, The chemical complexities of plutonium, Los Almos Sci. (2000) 364–381.

[18] J.A. Schramke, E.F.U. Santillan, R.T. Peake, Plutonium oxidation states in the waste isolation pilot plant repository, Appl. Geochem. 116 (2020) 104561, https://doi.org/10.1016/j.apgeochem.2020.104561.

[19] T. Rabung, T. Stumpf, H. Geckeis, R. Klenze, J.I. Kim, Sorption of Am(III) and Eu (III) onto γ-alumina: experiment and modelling, Radiochim. Acta 88 (2000) 711–716, https://doi.org/10.1524/ract.2000.88.9-11.711.

[20] M. Eibl, S. Virtanen, F. Pischel, F. Bok, S. Lönnrot, S. Shaw, N. Huittinen, A spectroscopic study of trivalent cation (Cm^{3+} and Eu^{3+}) sorption on monoclinic zirconia (ZrO_2), Appl. Surf. Sci. 487 (2019) 1316–1328, https://doi.org/10.1016/j.apsusc.2019.05.012.

[21] S. Virtanen, S. Meriläinen, M. Eibl, T. Rabung, J. Lehto, N. Huittinen, Sorption competition and kinetics of trivalent cations (Eu, Y and Cm) on corundum (α-Al_2O_3): a batch sorption and TRLFS study, Appl. Geochem. 92 (2018) 71–81, https://doi.org/10.1016/j.apgeochem.2018.02.011.

[22] K. Molodtsov, S. Schymura, J. Rothe, K. Dardenne, M. Schmidt, Sorption of Eu(III) on Eibenstock granite studied by μ-TRLFS: a novel spatially-resolved luminescence-spectroscopic technique, Sci. Rep. 9 (2019) 6287, https://doi.org/10.1038/s41598-019-42664-2.

[23] D. Pan, F. Fan, Y. Wang, P. Li, P. Hu, Q. Fan, W. Wu, Retention of Eu(III) in muscovite environment: batch and spectroscopic studies, Chem. Eng. J. 330 (2017) 559–565, https://doi.org/10.1016/j.cej.2017.07.184.

[24] T. Kupcik, T. Rabung, J. Lützenkirchen, N. Finck, H. Geckeis, T. Fanghänel, Macroscopic and spectroscopic investigations on Eu(III) and Cm(III) sorption onto bayerite (β-$Al(OH)_3$) and corundum (α-Al_2O_3), J. Colloid Interface Sci. 461 (2016) 215–224, https://doi.org/10.1016/j.jcis.2015.09.020.

[25] M. Demnitz, K. Molodtsov, S. Schymura, A. Schierz, K. Müller, F. Jankovsky, V. Havlova, T. Stumpf, M. Schmidt, Effects of surface roughness and mineralogy on the sorption of Cm(III) on crystalline rock, J. Hazard. Mater. 423 (2022) 127006, https://doi.org/10.1016/j.jhazmat.2021.127006.

[26] N. Huittinen, T. Rabung, P. Andrieux, J. Lehto, H. Geckeis, A comparative batch sorption and time-resolved laser fluorescence spectroscopy study on the sorption of Eu(III) and Cm(III) on synthetic and natural kaolinite, Radiochim. Acta 98 (2010) 613–620, https://doi.org/10.1524/ract.2010.1761.

[27] T. Yuan, S. Schymura, T. Bollermann, K. Molodtsov, P. Chekhonin, M. Schmidt, T. Stumpf, C. Fischer, Heterogeneous sorption of radionuclides predicted by crystal surface nanoroughness, Environ. Sci. Technol. 55 (2021) 15797–15809, https://doi.org/10.1021/acs.est.1c04413.

[28] J. Schabernack, I. Kurganskaya, C. Fischer, A. Luttge, Influence of muscovite (001) surface nanotopography on radionuclide adsorption studied by kinetic Monte Carlo simulations, Minerals 11 (2021) 468, https://doi.org/10.3390/min11050468.

[29] M. Stockmann, J. Schikora, D.A. Becker, J. Flügge, U. Noseck, V. Brendler, Smart Kd-values, their uncertainties and sensitivities - applying a new approach for realistic distribution coefficients in geochemical modeling of complex systems, Chemosphere 187 (2017) 277–285, https://doi.org/10.1016/j.chemosphere.2017.08.115.

[30] D.A. Dzombak, F.M.M. Morel, Surface Complexation Modeling: Hydrous Ferric Oxide, John Wiley & Sons,, 1990.

[31] J.W. Tonkin, L.S. Balistrieri, J.W. Murray, Modeling sorption of divalent metal cations on hydrous manganese oxide using the diffuse double layer model, Appl. Geochem. 19 (2004) 29–53, https://doi.org/10.1016/S0883-2927(03)00115-X.

[32] S.S. Mathur, D.A. Dzombak, Chapter 16 - Surface complexation modeling: Goethite, in: Interface Science and Technology, J. Lützenkirchen (Ed.), Surface Complexation Modeling, Elsevier, 2006: pp. 443–468. https://doi.org/10.1016/S1573-4285(06)80060-8.

[33] A.K. Karamalidis, D.A. Dzombak, Surface Complexation Modeling Gibbsite, Wiley,, 2010.

[34] S. Stumpf, T. Stumpf, C. Walther, D. Bosbach, T. Fanghänel, Sorption of Cm(III) onto different Feldspar surfaces: a TRLFS study, Radiochim. Acta 94 (2006) 243–248, https://doi.org/10.1524/ract.2006.94.5.243.

[35] P. Li, H. Wu, J. Liang, Z. Yin, D. Pan, Q. Fan, D. Xu, W. Wu, Sorption of Eu(III) at feldspar/water interface: Effects of pH, organic matter, counter ions, and temperature, Radiochim. Acta 105 (2017) 1049–1058, https://doi.org/10.1515/ract-2017-2797.

[36] J. Neumann, H. Brinkmann, S. Britz, J. Lützenkirchen, F. Bok, M. Stockmann, V. Brendler, T. Stumpf, M. Schmidt, A comprehensive study of the sorption mechanism and thermodynamics of f-element sorption onto K-feldspar, J. Colloid Interface Sci. 591 (2021) 490–499, https://doi.org/10.1016/j.jcis.2020.11.041.

[37] V. Brendler, A. Vahle, T. Arnold, G. Bernhard, T. Fanghänel, RES^3T - Rossendorf expert system for surface and sorption thermodynamics, J. Contam. Hydrol. 61 (2021) 281–291, https://doi.org/10.1016/S0169-7722(02)00129-8.

[38] B. Allard, G.W. Beall, Sorption of americium on geologic media, J. Environ. Sci. Heal. Part A Environ. Sci. Eng. 14 (1979) 507–518, https://doi.org/10.1080/10934527909374895.

[39] H. Chihara, C. Koike, Infrared absorption spectra of plagioclase feldspar: dependencies of composition and temperature, Planet. Space Sci. 149 (2017) 94–99, https://doi.org/10.1016/j.pss.2017.06.003.

[40] A.L. Polaczyk, J.E. Amburgey, A. Alansari, J.C. Poler, M. Propato, V.R. Hill, Calculation and uncertainty of zeta potentials of microorganisms in a 1:1 electrolyte with a conductivity similar to surface water, Colloids Surf. A Physicochem. Eng. Asp. 586 (2020) 124097, https://doi.org/10.1016/j.colsurfa.2019.124097.

[41] E.P. Poeter, M.C. Hill, D. Lu, C. Tiedeman, S.W. Mehl, UCODE_2014, with new capabilities to define parameters unique to predictions, calculate weights using simulated values, estimate parameters with SVD, evaluate uncertainty with MCMC, and more, Golden, Colorado School of Mines, 2014.

[42] J.C. Westall, FITEQL, A computer program for determination of chemical equilibrium constants from experimental data., 1982.

[43] N. Edelstein, R. Klenze, T. Fanghänel, S. Hubert, Optical properties of Cm(III) in crystals and solutions and their application to Cm(III) speciation, Coord. Chem. Rev. 250 (2006) 948–973, https://doi.org/10.1016/j.ccr.2006.02.004.

[44] T. Kimura, G.R. Choppin, Luminescence study on determination of the hydration number of Cm(III), J. Alloy. Compd. 214 (1994) 313–317, https://doi.org/10.1016/0925-8388(94)90921-0.

[45] A. Stefánsson, S. Arnórsson, Feldspar saturation state in natural waters, Geochim. Cosmochim. Acta 64 (2000) 2567–2584, https://doi.org/10.1016/S0016-7037(00)00392-6.

[46] D.L. Parkhurst, C.A.J. Appelo, Description of input and examples for PHREEQC version 3: a computer program for speciation, batch-reaction, one-dimensional transport, and inverse geochemical calculations, Reston, VA, U. S. Geol. Surv. (2013), https://doi.org/10.3133/tm6A43.

[47] D. Lu, M. Ye, M.C. Hill, E.P. Poeter, G.P. Curtis, A computer program for uncertainty analysis integrating regression and Bayesian methods, Environ. Model. Softw. 60 (2014) 45–56, https://doi.org/10.1016/j.envsoft.2014.06.002.

[48] S. Jenkins, W. Stumm, C. Huang, Specific chemical interaction affecting the stability of dispersed systems, Croat. Chem. Acta 42 (1970) 223–245.

[49] C.P. Huang, W. Stumm, Specific adsorption of cations on hydrous γ-Al_2O_3, J. Colloid Interface Sci. 43 (1973) 409–420, https://doi.org/10.1016/0021-9797(73)90387-1.

[50] P.W. Schindler, H. Gamsjäger, Acid-base reactions of TiO_2 (Anatase) - water interface and the point of zero charge of TiO_2 suspensions, Kolloid-Z. Und Z. Polymere 250 (1972) 759–763.

[51] J. Lützenkirchen, Surface Complexation Modelling, Elsevier Ltd,, 2006.

[52] S. Goldberg, Use of surface complexation models in soil chemical systems, Adv. Agron. (1992).

[53] R. Rahnemaie, T. Hiemstra, W.H. Van Riemsdijk, A new surface structural approach to ion adsorption: tracing the location of electrolyte ions, J. Colloid Interface Sci. 293 (2006) 312–321, https://doi.org/10.1016/j.jcis.2005.06.089.

[54] J. Vuceta, Adsorption of Pb(II) and Cu(II) on α-Quartz from Aqueous Solutions: Influence of pH, Ionic Strength, and Complexing Ligands. Diss. (Ph. D.), California Institute of Technology, 1976, 10.7907/71AV-TE55.

[55] E.S. Chardon, F.R. Livens, D.J. Vaughan, Reactions of feldspar surfaces with aqueous solutions, Earth-Sci. Rev. 78 (2006) 1–26, https://doi.org/10.1016/j.earscirev.2006.03.002.

[56] W.H. Casey, H.R. Westrich, G.R. Holdren, Dissolution rates of plagioclase at pH= 2 and 3, Am. Mineral. 76 (1991) 211–217.

[57] J. Lützenkirchen, A. Abdelmonem, R. Weerasooriya, F. Heberling, V. Metz, R. Marsac, Adsorption of dissolved aluminum on sapphire-c and kaolinite:

implications for points of zero charge of clay minerals, Geochem. Trans. 15 (2014) 1–14, https://doi.org/10.1186/1467-4866-15-9.
[58] J.E. Stubbs, B.A. Legg, S.S. Lee, P. Dera, J.J. De Yoreo, P. Fenter, P.J. Eng, Epitaxial growth of gibbsite sheets on the basal surface of muscovite mica, J. Phys. Chem. C. (2019), https://doi.org/10.1021/acs.jpcc.9b08219.
[59] B.A. Legg, M.D. Baer, J. Chun, G.K. Schenter, S. Huang, Y. Zhang, Y. Min, C. J. Mundy, J.J. De Yoreo, Visualization of aluminum ions at the mica water interface links hydrolysis state-to-surface potential and particle adhesion, J. Am. Chem. Soc. 142 (2020) 6093–6102, https://doi.org/10.1021/jacs.9b12530.
[60] T. Hiemstra, H. Yong, W.H. Van Riemsdijk, Interfacial charging phenomena of aluminum (Hydr)oxides, Langmuir 15 (1999) 5942–5955, https://doi.org/10.1021/la981301d.
[61] J.N. Kondo, E. Yoda, H. Ishikawa, F. Wakabayashi, K. Domen, Acid property of silanol groups on zeolites assessed by reaction probe IR study, J. Catal. 191 (2000) 275–281, https://doi.org/10.1006/jcat.1999.2807.
[62] E.J.M. Hensen, D.G. Poduval, P.C.M.M. Magusin, A.E. Coumans, J.A.R. va. Veen, Formation of acid sites in amorphous silica-alumina, J. Catal. 269 (2010) 201–218, https://doi.org/10.1016/j.jcat.2009.11.008.
[63] T. Stumpf, C. Hennig, A. Bauer, M.A. Denecke, T. Fanghänel, An EXAFS and TRLFS study of the sorption of trivalent actinides onto smectite and kaolinite, Radiochim. Acta 92 (2004) 133–138, https://doi.org/10.1524/ract.92.3.133.30487.
[64] E. Hartmann, B. Baeyens, M.H. Bradbury, H. Geckeis, T. Stumpf, A Spectroscopic characterization and quantification of M(III)/clay mineral outer-sphere complexes, Environ. Sci. Technol. 42 (2008) 7601–7606, https://doi.org/10.1021/es801092f.
[65] M. Schmidt, T. Stumpf, M.M. Fernandes, C. Walther, T. Fanghänel, Charge compensation in solid solutions, Angew. Chem. - Int. Ed. 47 (2008) 5846–5850, https://doi.org/10.1002/anie.200705827.
[66] T. Stumpf, A. Bauer, F. Coppin, T. Fanghänel, J.I. Kim, Inner-sphere, outer-sphere and ternary surface complexes: a TRLFS study of the sorption process of Eu(III) onto smectite and kaolinite, Radiochim. Acta 90 (2002) 345–349, https://doi.org/10.1524/ract.2002.90.6.345.

Natural and synthetic plagioclases: Surface charge characterization and sorption of trivalent lanthanides (Eu) and actinides (Am, Cm)

J. Lessing [a], J. Neumann [a,≠], J. Lützenkirchen [b], F. Bok [a], S. Moisei-Rabung [b], D. Schild[b], V. Brendler [a], T. Stumpf [a], M. Schmidt [a,*]

[a] *Helmholtz-Zentrum Dresden-Rossendorf (HZDR), Bautzner Landstraße 400, 01328 Dresden, Germany*

[b] *Karlsruher Institut für Technologie (KIT), Hermann-von-Helmholtz-Platz 1, 76344 Eggenstein-Leopoldshafen, Germany*

[≠] *Current Address: Argonne National Laboratory, 9700 South Cass Ave, Lemont, IL 60439, USA*

* *Corresponding Author, E-Mail address:* moritz.schmidt@hzdr.de

Jessica Lessing: j.lessing@hzdr.de, ORCID: 0000-0002-6485-4035

Julia Neumann: jneumann@anl.gov, ORCID: 0000-0002-3650-3967

Johannes Lützenkirchen: johannes.luetzenkirchen@kit.edu

Frank Bok: f.bok@hzdr.de, ORCID: 0000-0002-6885-2619

Silvia Moisei-Rabung: silvia.moisei-rabung@kit.edu

Dieter Schild, dieter.schild@kit.edu

Vinzenz Brendler: v.brendler@hzdr.de, ORCID: 0000-0001-5570-4177

Thorsten Stumpf: t.stumpf@hzdr.de, ORCID: 0000-0002-4505-3865

Moritz Schmidt: moritz.schmidt@hzdr.de, ORCID: 0000-0002-8419-0811

Content

1. Mineral characterization

- **Phase impurities**

PXRD (Rigaku MiniFlex600 PDXL; Reference: ICCD Database, PDXL 2, Version 4.21.0.2)

Table S1. Determined mineral phases of investigated feldspars via PXRD.

Mineral	Main component	Minor contributes
synthetic Anorthite	100 % Anorthite (calcium tecto-dialumodisilicate) PDF 01-086-1705	-
natural Labradorite	100 % Labradorite PDF 05-001-0013	-
natural Oligoclase	79% Albite, Ca-bearing PDF 04-017-0892 20 % Anorthite, Na-bearing, syn PDF 01-083-6377	1 % Quartz, syn PDF 04-008-7652

- **Specific surface area (SSA)**

SSA was determined by N_2 physisorption using a Quantachrome Nova Station A. A 23 points standard measurement was performed and the observed isotherm was analyzed using the method of Brunauer, Emmet, and Teller (BET). Degassing of the samples was done for 3 h at 150 °C.

Table S2. Overview of batch experiments used to develop the SCM (pH 4 – 9). Grain size < 63 µm

Experiment No		Mineral	M^{3+}	$[M^{3+}]$ / µM	Ionic strength / M (Electrolyte)	Solid to liquid ratio (SLR) / g/L	Carbonate free	Number of samples (n)
I Electrophoretic mobility	1	Labradorite (An_{79})	-	-	0.1 (NaCl)	0.2	no	11
	2	syn. Anorthite	-	-	0.1 (NaCl)	0.2	no	12
	3	Oligoclase	-	-	0.1 (NaCl)	0.2	no	13
	4	K-feldspar*	-	-	0.1 (NaCl)	0.2	no	11
	5	K-feldspar	Al^{3+}	5	0.1 (NaCl)	0.2	no	15
	6	K-feldspar	Al^{3+}	10	0.1 (NaCl)	0.2	no	15
	7	K-feldspar	Ca^{2+}	25	0.1 (NaCl)	0.2	no	15
	8	K-feldspar	Ca^{2+}	36	0.1 (NaCl)	0.2	no	15
II Streaming potential	1	syn. Anorthite	-	-	0.002 ($CaCl_2$)	0.5	yes	1
	2	syn. Anorthite	-	-	0.002 ($CaCl_2$)	2	yes	1
	3	syn. Anorthite	-	-	0.002 ($CaCl_2$)	2	yes	1
	4	syn. Anorthite	-	-	0.002 ($CaCl_2$)	2	yes	1
	5	syn. Anorthite	-	-	0.005 (NaCl)	2	yes	1
	6	syn. Anorthite	-	-	0.005 (NaCl)	2	yes	1
	7	syn. Anorthite	-	-	0.005 (NaCl)	2	yes	1
	8	syn. Anorthite	-	-	0.005 (NaCl)	2	yes	1
	9	syn. Anorthite	-	-	0.002 ($CaCl_2$)	2	yes	1
	10	syn. Anorthite	-	-	0.002 ($CaCl_2$)	2	yes	1
III Batch	1	Labradorite (An_{79})	Eu	10	0.1 (NaCl)	3.0	no	25
	2	Labradorite	Am	0.052	0.01 (NaCl)	3.0	yes	10
	3	K-feldspar*	Eu	10	0.1 (NaCl)	3.0	no	20

	4	**K-feldspar***	**Am**	0.052	0.01 (NaCl)	3.0	yes	19
	5	**Oligoclase (An_{23})**	**Eu**	10	0.1 (NaCl)	3.0	no	15
	6	**Oligoclase**	**Am**	0.052	0.01 (NaCl)	3.0	yes	16
	7	**syn. Anorthite(An_{99})**	**Eu**	10	0.1 (NaCl)	3.0	no	1526
	8	**syn. Anorthite**	**Am**	0.052	0.01 (NaCl)	3.0	yes	11
IV TRLFS	**1**	**syn. Anorthite**	**Cm**	0.5	0.1 (NaCl)	3.0	yes	37

47 * Neumann et al. 2021 [4]

2. Determination of Input Parameters for SCM

2.1. Calculation of Surface Site Density (SSD)

The common oxygen-containing mineral phases will form a layer of hydroxylic groups on their surface when they are in equilibrium with water (liquid or vapor). These hydroxylic groups act as binding sites in sorption reactions. To quantify their amount/concentration with respect to mineral SSA and the systems SLR, a value for the SSD must be available. There are several ways to determine the SSD of a mineral:

- Experimentally determined (e.g. tritium exchange)
- Calculated (from crystallographic data)
- Fitted from other batch experiments (e.g. acid/base titrations)
- Chemical analogues / estimation / assumption

All options have their individual justification but lead to a wide range of SSD values in the literature. Many of these datasets are chemically unrealistic and thus work for their specific experimental conditions only. For a reference data set, however, it must be ensured that the data set not only performs under the specific conditions of the measurement of its creation, but that a reasonably realistic value is determined, which also works under other conditions (e.g. other sorption scenarios, different chemical conditions, degree of grinding, ageing). The method to obtain SSD from crystallographic calculation is preferred because it excludes experimental uncertainty or effects due to sample preparation.

For this purpose, the morphology of the mineral and thus the real surface planes of the mineral must be known. In case of a mineral with unknown morphology, the Bravais-Friedel-Donnay-Harker (BFDH) [1] method can be used to calculate the morphology with the most stable surface planes from crystallographic data [1]. For each surface plane, the number of hydroxylic groups per area unit can be determined using the following approach:

1. Calculation of surface planes from crystal structure data [2]. The software used was "Mercury CSD" [3]
2. Outermost oxygen atoms are handled as hydroxylic surface groups that are active in site-binding (surface complexation) models.
3. Creation of a surface cell built from four crystallographically identical oxygen atoms.
4. Measuring of the atom distances and calculation of the cell area (measured in nm^2).
5. Determining the number of all oxygen atoms within the surface cell. Oxygen atoms in one corner of the surface cell count as quarters, oxygen atoms at the edge of the surface cell count as half.
6. The SSD for a single plane is then calculated as the proportional sum of all reactive oxygen atoms $SSD_{HKL} = O_{plane} + ¼\ O_{corner} + ½\ O_{edge}$
7. Repetition of that procedure for all planes and calculation of a mean overall SSD value with respect to the surface planes area ratios.

Anorthite can form a variety of morphologies. The most important crystal surfaces are {001} ≡ {00−1}, {010} ≡ {0−10}, {10−1} ≡ {−101}, {100} ≡ {−100} and {0−11} ≡ {01−1}. This is in good agreement with the surface planes from the morphology calculation using the crystallographic data [2]. As an example, **Figure S1** shows the {001}/{00−1} crystal surface

with a surface cell consisting of four identical oxygen atoms including other surface oxygen atom positions.

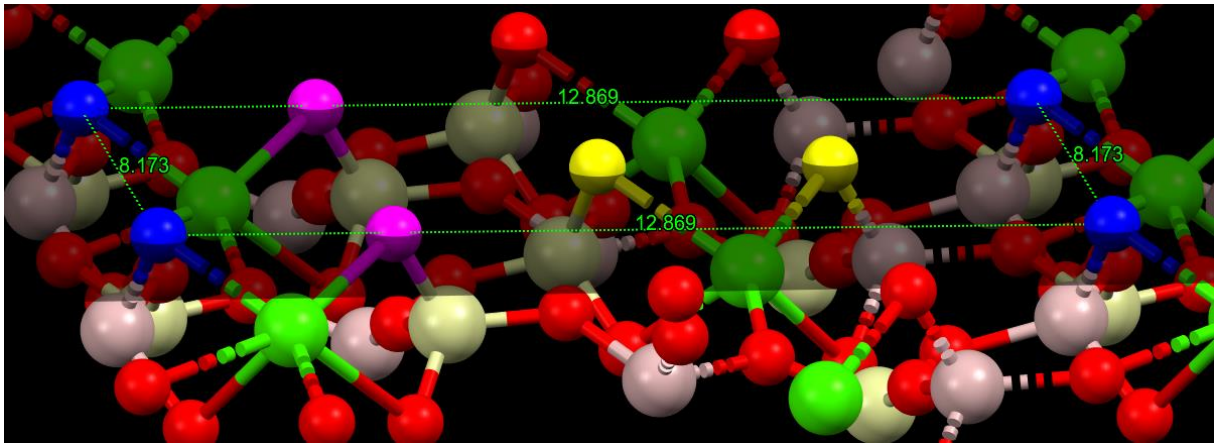

Figure S1. Anorthite {001}/{00−1} crystal surface with a surface cell consisting of four identical oxygen atoms (blue) including other surface oxygen atom positions at the surface cell edges (pink) and inside the surface cell (yellow). The dimension of the surface cell is given here in Ångström due to the software conditions.

The calculated SSD values for all calculated individual areas as well as their relative area ratios are given in **Table S2**.

Table S3 Overview of considered anorthite surface planes and their relative area ratio and SSD for determination of an average SSD for anorthite based on crystallographic data.

Surface planes	**Relative area ratio**	**Plane's SSD [nm^{-2}]**
{001} ≡ {00−1}	2 × 0.168	3.806
{010} ≡ {0−10}	2 × 0.182	3.455
{10−1} ≡ {−101}	2 × 0.094	4.217
{100} ≡ {−100}	2 × 0.030	3.840
{0−11 ≡ {01−1}	2 × 0.001	5.139

An overall SSD value was obtained by calculating the mean value from the individual SSD values of the crystal surfaces, taking into account the relative area ratios. This overall SSD value for anorthite equals 3.74 nm^{-2} and is quite close to the SSD value of 3.304 nm^{-2} of orthoclase from previous investigations [4].

2.2. Calculation of site occupancy

First, the site density (SD) in [sites/l] was calculated from the surface site density (SSD), the specific surface area (SSA) and the solid-liquid ratio (SLR) of the mineral via the following equation.

$$SD = SSA\left[\frac{m^2}{g}\right] \cdot SLR\left[\frac{g}{l}\right] \cdot SSD\left[\frac{sites}{m^2}\right]$$

As a bidentate coordination of M^{3+} was assumed [5], the value of SD was divided by 2.

The number of M^{3+} ions $N(M^{3+})$ in solution (in [ions/l]) was calculated via:

$$N(M^{3+})\ [\frac{atoms}{l}] = \ c(M^{3+})\left[\frac{mol}{l}\right] \cdot N_A\left[\frac{1}{mol}\right]$$

with N_A being the Avogadro constant.

The site : M^{3+} ratio was calculated by dividing SD in [sites/l] by $N(M^{3+})$.

3. Electrophoretic mobility and mineral dissolution measurements

For further analysis, aqueous Al and Ca concentrations in the feldspar suspension were measured by ICP-MS after 24 h in 0.1 M NaCl aqueous solution, see figure S2. For each feldspar different amounts of these ions are present in solution. Anorthite shows the highest concentration of Ca and Al, labradorite has a smaller amount of these ions in solution, while oligoclase as well as K-feldspar release almost no Al/Ca ions into solution. To conclude, feldspar dissolution increases with Ca content. Uncertainties correspond to a 68% confidence level (1 σ).

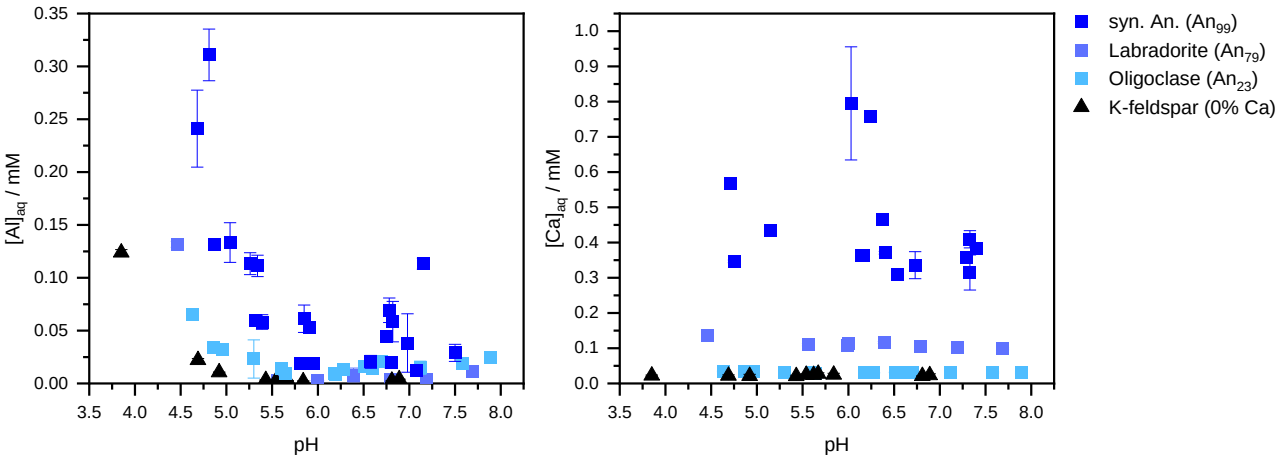

Figure S2. Concentrations of a) [Ca^{2+}] and b) [Al^{3+}] measured in solution of selected samples series (c.f. **Table S2** Exp. III/1,3,6 and 8).

In **Figure S3**, the aluminum concentration in solution as a function of pH is displayed as well as the calculated solubility curve of gibbsite ($Al(OH)_3$). It is seen that all K-feldspar samples with a different amount of added Al^{3+} show a similar curve with a solubility minimum at pH 6. Regarding the speciation of Al, amorphous, solid aluminum hydroxide ($Al(OH)_3$) is dominating under these conditions.

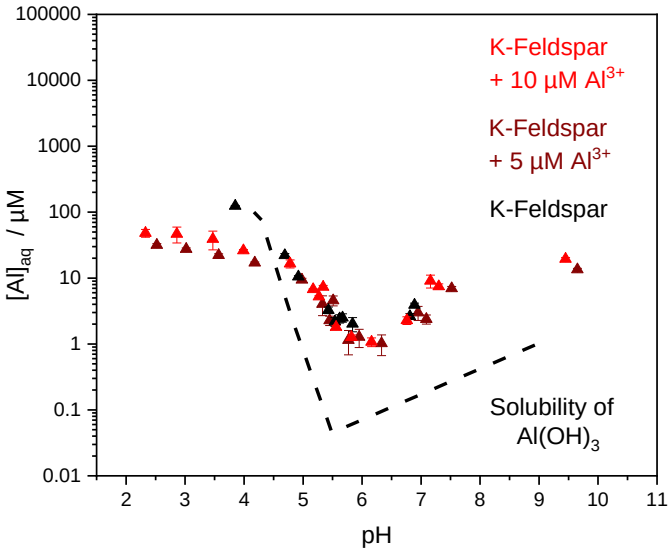

Figure S3. Concentration of Al^{3+} measured in solution of selected sample series (c.f. **Table S2** Exp III/1,3,5 and 7).

The electrophoretic mobility of K-feldspar with different amounts of Ca^{2+} is shown in **Figure S4** (in comparison to the data of K-feldspar with different amounts of Al^{3+} shown in section 3.1.1 of the main section). Although the Ca concentration is higher than in the Al experiments, its impact on the electrophoretic mobility is significantly lower.

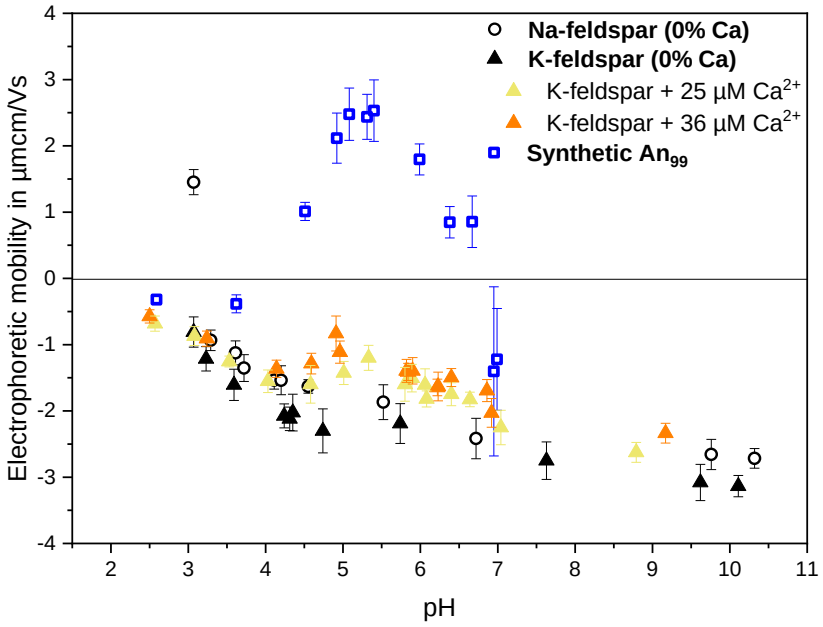

Figure S4. Electrophoretic mobility measured of K-feldspar with different amounts of added $CaCl_2$ (c. f. Table S1 Exp. I/1-4; 7-8).

4. Investigation of Al Phase

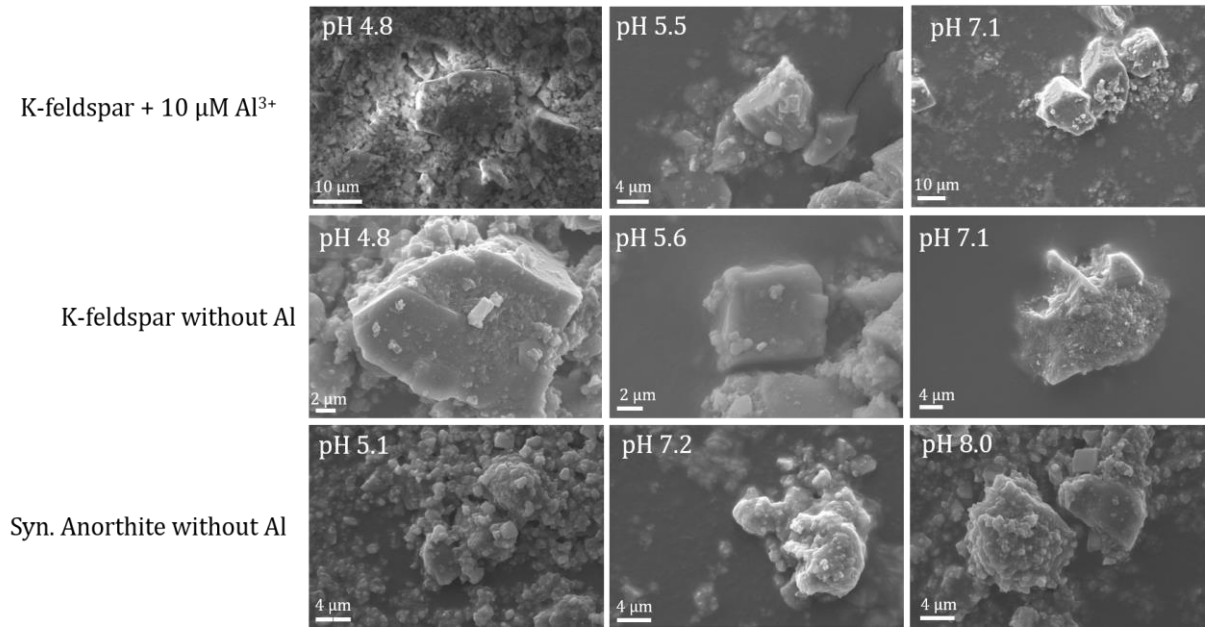

Figure S5. SEM pictures of mineral samples with different amount of added Al^{3+}.

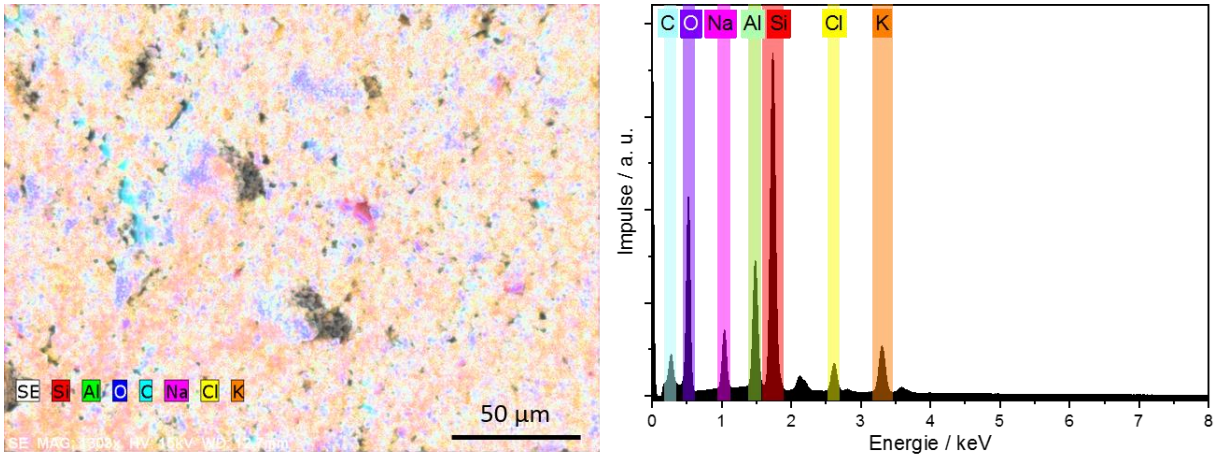

Figure S6. EDX results of K-feldspar with 10 µM Al^{3+}; left: with SEM scanned surface and distribution of elements Si (red), Al (green), O (dark blue), C (turquoise), Na (pink), Cl (yellow) and K (orange); right: corresponding energy spectrum.

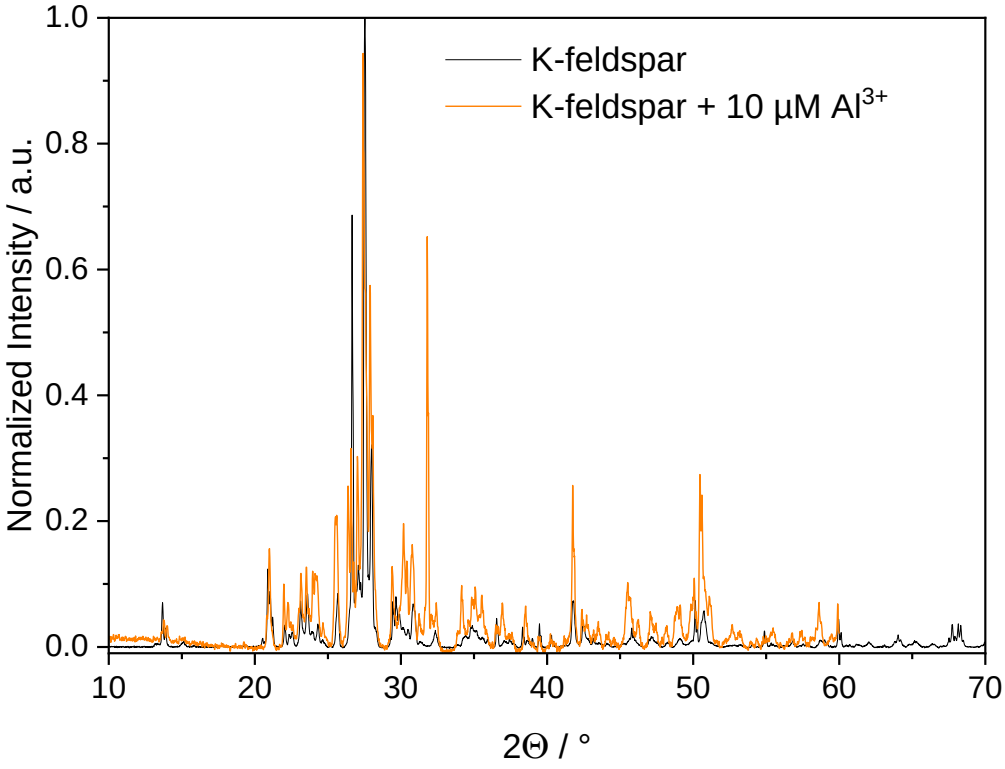

Figure S7. PXRD measurements of pure K-feldspar (black) and with Al^{3+} treated K-feldspar (orange). No new phase could be identified.

5. Streaming potential

5.1.1. Streaming experiments

Figure S8 shows a selection of the streaming potential data in both Ca and Na chloride solution at the same nominal ionic strength. Clearly the behavior in Ca solution is different from Na: the isoelectric point in the Ca solution is higher, and the height of the maximum at around pH 5 is above that for Na. This points to an effect of Ca in the sense that it can interact with the anorthite surface. The ICP-OES data for Al and Si show that there is probably no significant difference in dissolution between Ca and Na systems (see Figure S10 and Figure S11). This corroborates the idea that (at least) both Ca and Al are affecting the zeta-potentials of anorthite, albeit with the stronger effect for Al. Figure 1d also shows that the dissolution does not significantly change the behavior of the anorthite sample. It is clear that the Na behavior can be reproduced after experiments with the Ca solution. Also the initial Ca behavior is retrieved after experiments with Na. This is further corroborated by the ICP-OES results which show roughly Al/Si ratios of unity as expected for stoichiometric dissolution.

An intuitive interpretation could involve that the dissolution affects the zeta-potential results by re-adsorption of dissolving ions and that this is a reversible process (i.e. the surface is not preferentially leached). In Na solution, the IEP is lower, and this IEP does not appear to depend significantly on the sodium concentration so that the obtained value of 6.8 can be used for a surface complexation model.

Additional streaming potential experiments were carried out with anorthite (see Figure S8). For each experiment a fresh solution with the annotated composition was used. In some cases (at the start with a new solid sample), measurements were carried out at the natural pH value (i.e. the respective salt solution) without adding acid or base. In the other cases, the pH of the solutions was increased by adding NaOH (0.1 M NaOH solution, in the case of NaCl solution) or $Ca(OH)_2$ powder (in the case of $CaCl_2$ solution) to increase the pH to pH > 9. Once the pH in the 500 ml reservoir was above pH 9 and stable for 15 minutes, the titration experiments with 0.1 M HCl was initiated. For the first data point, no HCl was added. The reservoir solution was under Ar atmosphere. Most experiments were carried out with the "standard" settings (i.e. 900 seconds rinse), while others (marked long) involved rinsing 3600 seconds, and again others (marked short) involved 300 seconds rinsing. At the end of most experiments, an aliquot of the acidic solution was used for elemental analysis. At the end of a series with one solid, the solid was used for XPS measurement. The original particles after grinding were also analyzed by XPS.

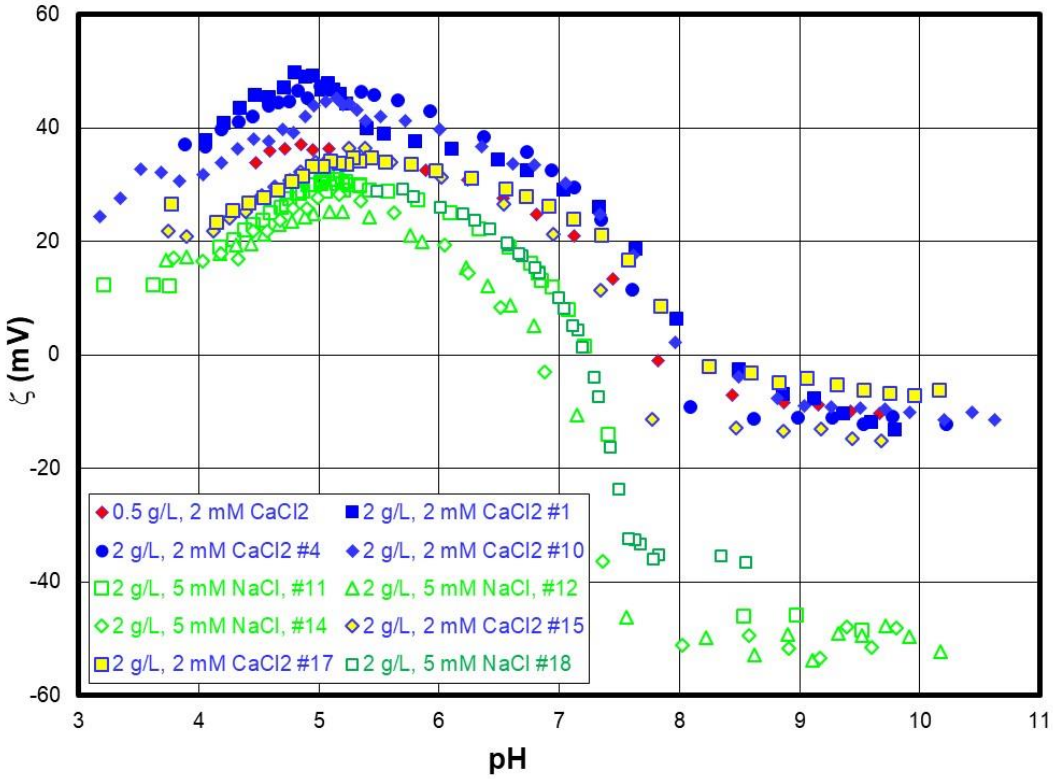

Figure S8. Streaming potential data in 2 mM $CaCl_2$ (blue framed full symbols) and 5 mM NaCl (green open symbols) solutions. The red symbols were obtained with a mass of 0.5 g in the cylindrical cell of the SurPass instruments. The other experimental results were obtained on the same sample of 2 g anorthite in the cylindrical cell. The numbers (#i) indicate the number of the experiment. Error bars are omitted for the sake of clarity. Standard deviations were below 3 mV for the data points on the figure as calculated from 6 measurements for each point shown.

Figure S9 shows the full set of results from the streaming potential measurements. It is clear that (as also discussed in the main text) the sodium chloride experiments clearly differ from the calcium chloride experiments. Interestingly, the initial measurements in calcium solutions coincide with the pH dependent measurements in NaCl. No clear trends with time or with rinsing time were observed.

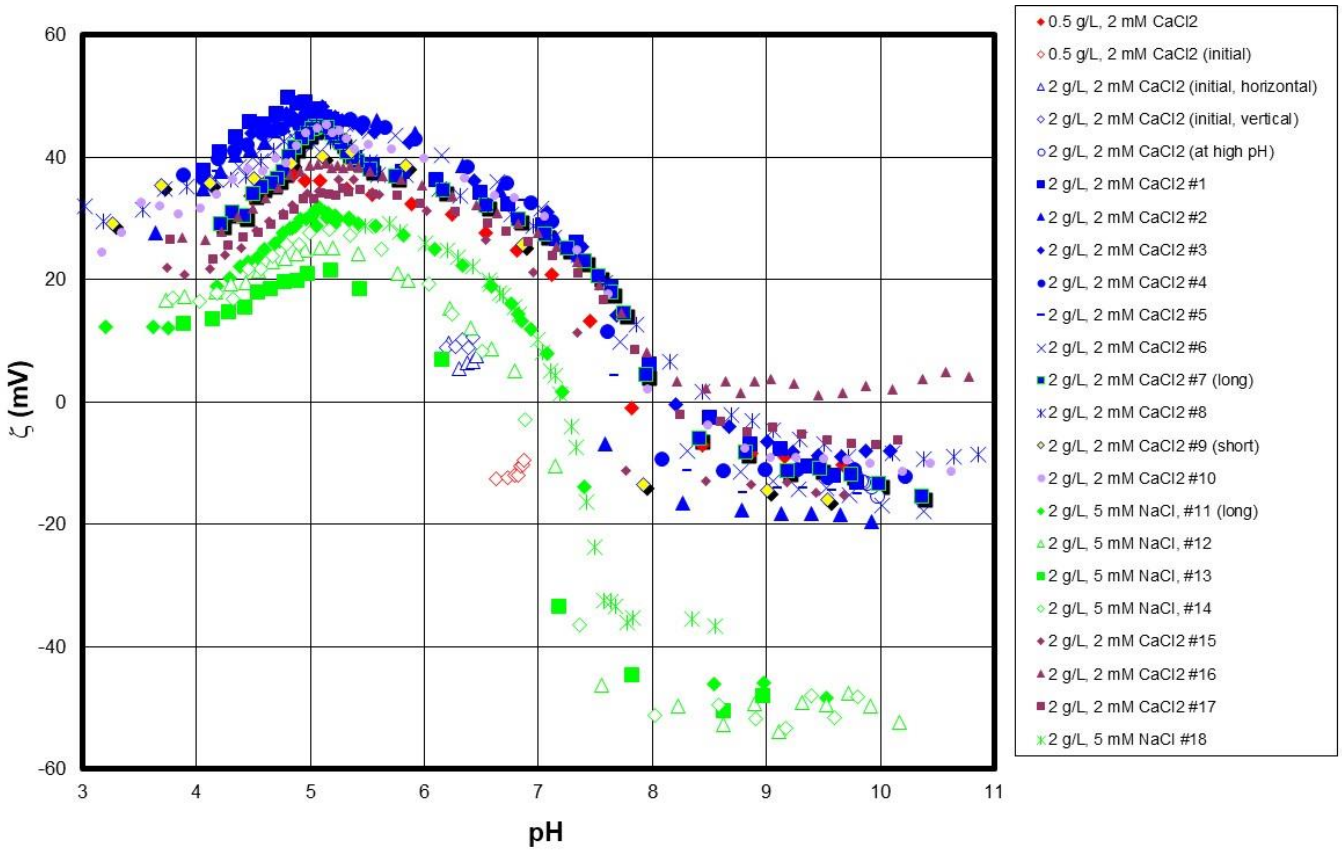

Figure S9. Series of streaming potential data for anorthite. The solid content in the cell is given, the solution composition is stated and the kind of experiments (with standard, i.e. no specific addition, short or long rinsing time) can be compared.

The clear distinction between sodium and calcium however is persistent, reproducible, and reversible.

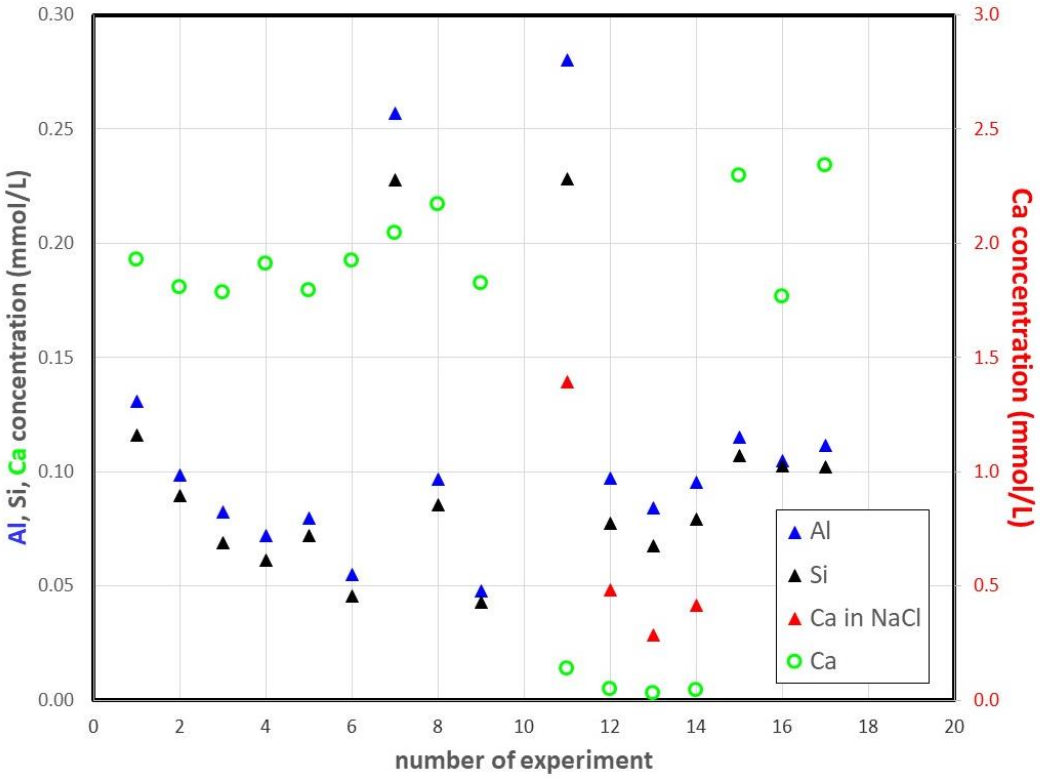

Figure S10. Measured solution compositions after the experiments with 2 g anorthite from Figure S9 as a function of the number of the experiment.

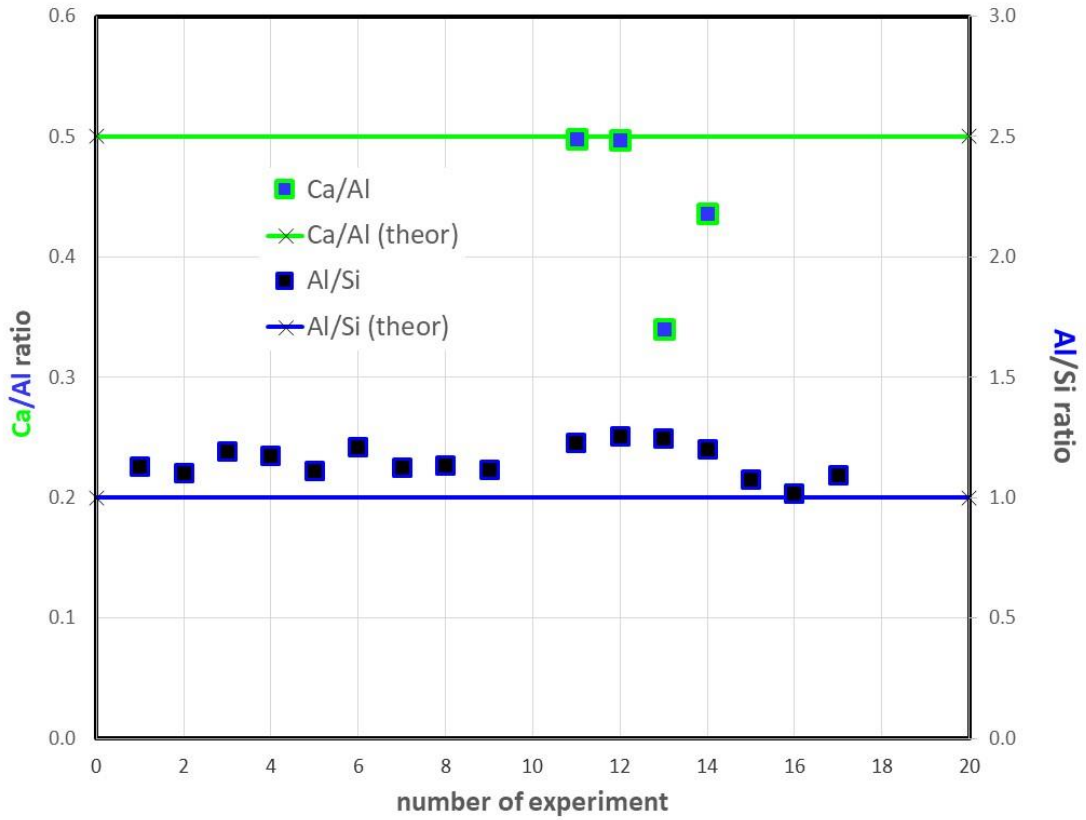

Figure S11. Concentration ratios calculated from solution compositions after the experiments with 2 g anorthite from Figure S9 as a function of the number of the experiment.

Figure S10 shows the solution composition after the runs according to the experiment numbers. The measurements by ICP-OES (Figure S11) indicate that the dissolution at the end of the experiment is more or less stoichiometric concerning Si and Al. For Ca no attempt was made to correct for the background salt, since this involves the difference of two large numbers and the associated large errors. Only for the Na dominated input solutions, we believe that we obtain reliable values of Ca/Al of about 0.5 (for two measurements) and below for the two other measurements. The value of 0.5 supports the statement about stoichiometric dissolution. The XPS spectra did not show any significant difference among the samples analyzed, which also confirms the absence of preferential leaching. This agrees with the reversible behavior between sodium and calcium based solutions inferred from streaming potential measurements. The XPS data in Table S4 support the idea that the solution data should not be overinterpreted. The experimental errors in both the solution concentration measurements and the XPS preclude a detailed discussion.

Table S4. XPS data for the anorthite surface. Original denotes the powder as synthesized. 0.5 g denotes the sample after the experiments with 0.5 g anorthite (from Figure S9) and 2 g (#18) after the series with 2 g anorthite.

	Ca/Al			Al/Si		
	powder	powder on In-foil	theory	powder	powder on In-foil	theory
original	0.5	0.4	0.5	1.2	1.1	1.0
0.5 g	0.4	0.5	0.5	1.2	1.2	1.0
2 g (#18)	0.4	0.5	0.5	1.0	0.9	1.0

The streaming potential measurements suggest that there is an effect of Ca on the charging of anorthite. Based on the experimental results in the main text, this is accompanied by effects of dissolved Al, which according to the solution compositions should be roughly the same for the two kinds of solution. No attempt was made to add Al to the solution.

5.1.2. Modeling zeta potential

The only experimental data that could be obtained for modelling the acid-base behavior were streaming potential results that yield zeta potentials. A compromise in terms of ionic strength (5 mM NaCl) was chosen, to (i) have the same kind of background salt as in the relevant sorption experiments, (ii) be in a concentration range, where dissolution does not affect the overall ionic strength, while at the same time obtaining sufficiently high zeta potentials, (iii) limit effects of surface conductivity, and (iv) obtain a sharp IEP. The obtained IEP of pH 6.8 agrees with the one obtained from both experimental data, suggesting that sodium interaction does not shift the IEP. To be consistent with previous modelling work within the same project, a diffuse layer model was chosen to simulate the zeta potentials from the streaming potential experiments.

6. Comparison of sorption edge and electrophoretic mobility

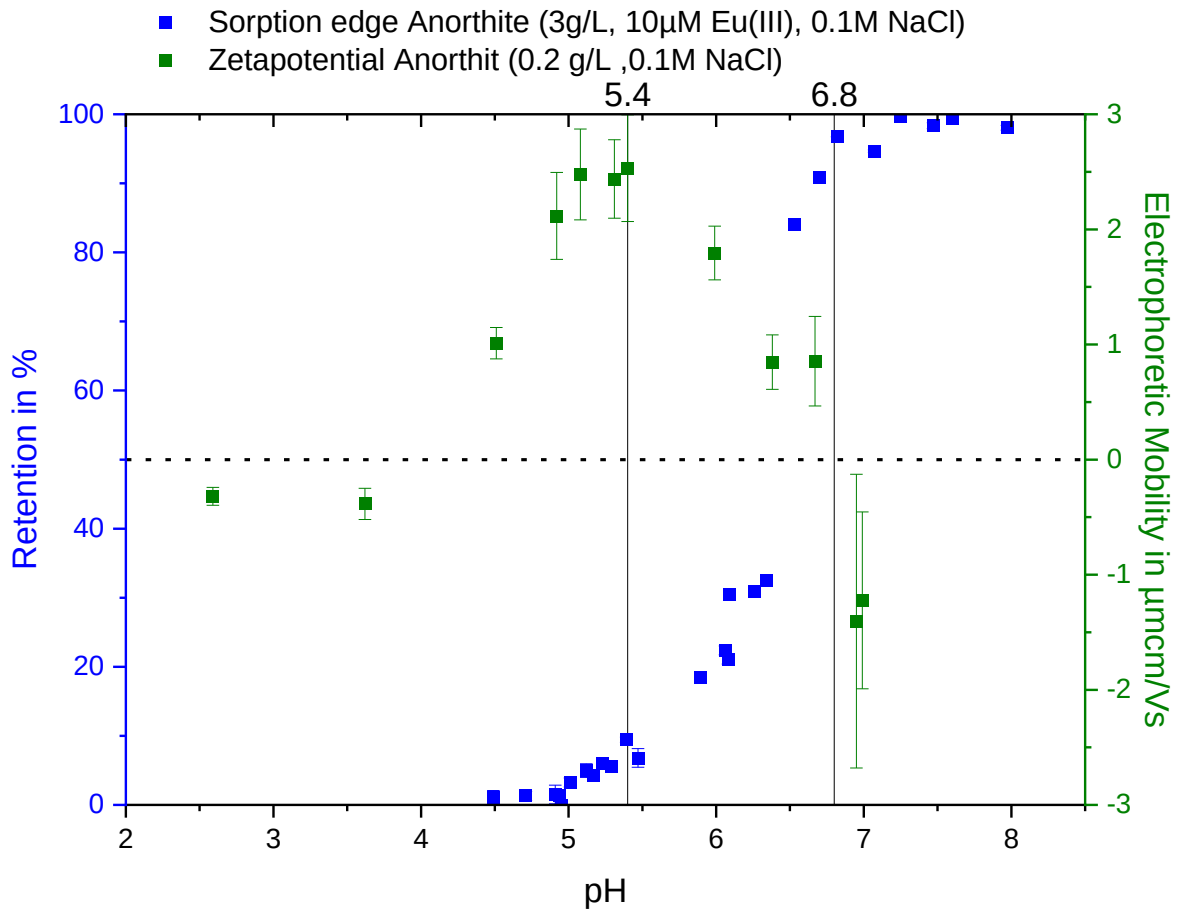

Figure S12. Retention of Eu on anorthite as well as the electrophoretic mobility on anorthite were plotted in one diagram.

The comparison of EM and Eu retention makes it obvious that the strong decrease of EM from pH 5.4 and the strong increase of sorption on anorthite are related to each other.

7. TRLFS

7.1. Peak deconvolution of Cm emission spectra

In section 4.3 of the main text, we discussed that the peak deconvolution of the emission spectra was not successful due to the simultaneous formation of two surface complexes. Figure S13 supports this statement by showing the deconvolution of two of the emission spectra at two different pH values, pH 4.99 and pH 5.24. The figures show the single component spectra obtained for the K-Feldspar [4] in black, red, and blue (translucent lines), as well as the measured sample spectra in black. The deconvoluted spectra (purple) are obtained by subtracting the spectrum of the Cm aquo ion (Species 1 in Figure S7) from the sample spectrum.

In the left part of Figure S7, it can be seen that there is only a minor red shift of the sample spectrum. Subtraction of 96 % Cm aquo ion results in the spectrum shown in purple. A minor contribution of Species 2 (red) can be identified, indicated by the overlap of the purple and red spectra, but the signal is too noisy to be used for further peak deconvolution. The next higher pH value (5.24, Figure S13 right) is obtained by subtracting 91 % Cm aquo ion from the sample spectrum and shows a less noisy deconvoluted spectrum. However, it clearly overlaps with both the red and blue spectrum, indicating contributions of both Species 2 and Species 3. Therefore, the deconvoluted spectrum is the sum of both species and we cannot extract the single component spectra for synthetic anorthite.

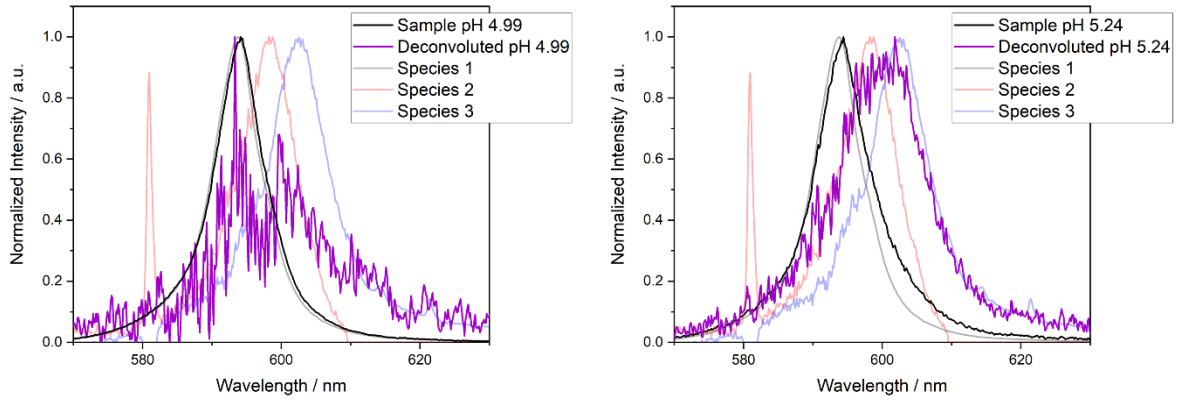

Figure S13. Peak deconvolution of Cm emission spectra of synthetic anorthite at two different pH values. Note that the signal at 580 nm corresponds to rare earth impurities in the single component spectra of the K-feldspar [4].

7.2. Determination of luminescence lifetimes

For further characterization of the surface complexes their luminescence lifetimes were determined. As already mentioned, it is not straightforward to determine exact values due to the simultaneous formation of surface species and the large number of different Cm species at a given pH. Nonetheless, the measured lifetimes could be fitted as a bi-exponential decay with using the least-squares fitting routine included in MATLAB using an in-house script. The fit produces reasonable lifetimes and agreement with measured data, if one lifetime is fixed at 68 µs for the Cm(III) aquo ion and only the relative composition and the second lifetime are allowed to vary. The aquo ion lifetime was fit for the lowest pH (5.01), for the highest pH (10.13) both lifetimes were fit.

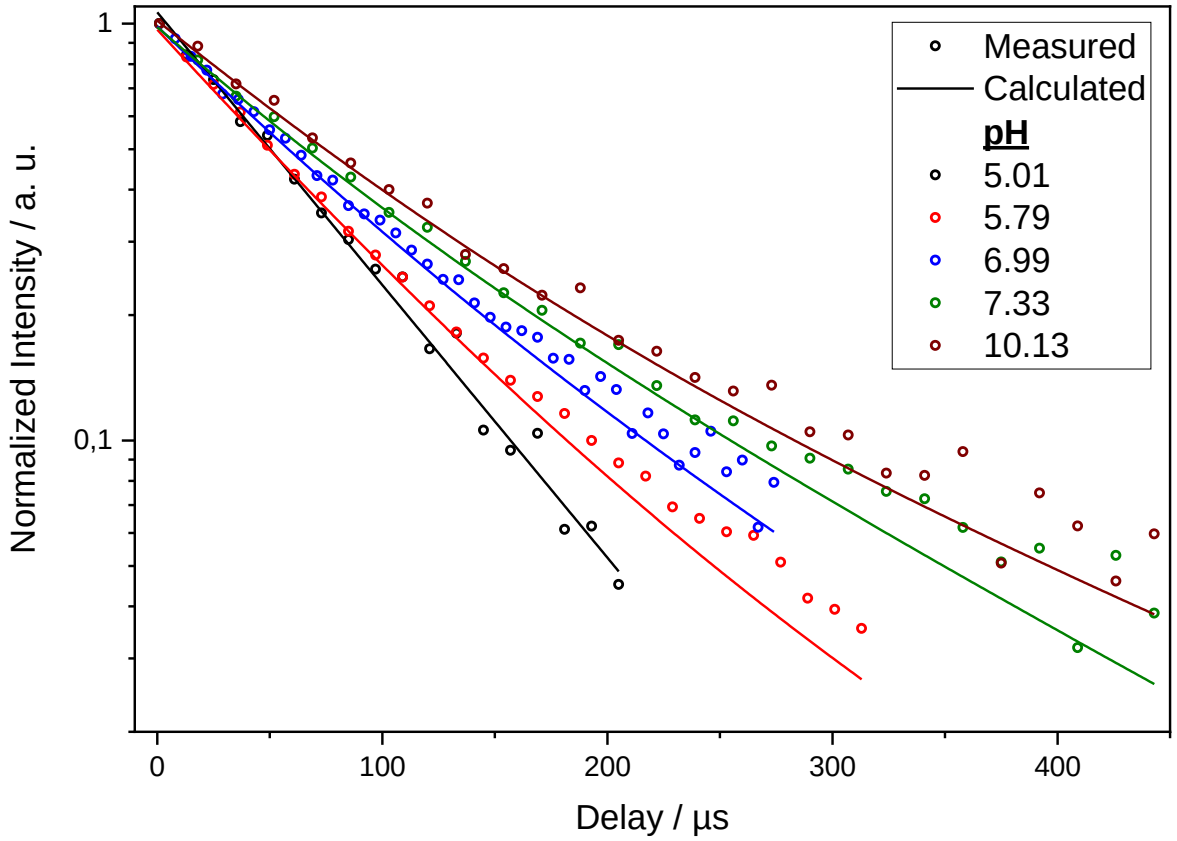

Figure S14. Life time measurements for five selected, representative pH values of synthetic anorthite (3 g/L) reacted with 0.5 µM Cm in 0.1 M NaCl as well as their calculated fit.

At pH 5, only small amount of sorption occurs and the Cm aquo dominates the speciation. Its well-known lifetime of 68 µs [6] was confirmed by the fitting results at pH 5.0. Cm(III) species 2 - 4 are present at higher pH. The lifetime analysis suggests the existence of at least two species with longer lifetimes between 140 - 150 µs. The amount of water molecules in the first coordination sphere of a curium ion can be calculated with the recorded luminescence decay constant k_{obs} and equation by Kimura [7] and its luminescence lifetime τ (in ms) as long as no other quenching entities than water are present.

$$n_{H_2O} = 0.65k_{obs} - 0.88 \quad \text{and} \quad k_{obs} = {}^{1}/_{\tau}$$

A lifetime of ~140 µs corresponds to four water molecules in the first coordination sphere of these species, in good agreement [8,9] with the assignment as inner sphere (IS) species based on the luminescence emission data. With increasing pH the peak deconvolution suggests the continuous hydrolysis of the IS sorption complex. The OH^- anion and water both show equivalent quenching efficiency via their O-H vibrations.[6] Consequently, the absence of a change in luminescence lifetime confirms that the observed red shift is caused by hydrolysis.

The evaluation of the data at pH > 10 reveals the existence of a fifth species with a lifetime of ~200 µs which can be assigned to an incorporation in the surface layers according to *Demnitz et al.*[9], who also showed that this rather corresponds to feldspars commonly form these surface incorporation species[9].

Table 2 sums up the fitted lifetimes as well as the amount of H_2O in the first coordination sphere calculated from them.

Table S5. Emission lifetime for the identified surfaces complexes as well as corresponding number of remaining water molecules in the first hydration shell of Cm ($n(H_2O)$).

Species	**Emission lifetime τ / µs**	**$n(H_2O)$**
Cm-Aquo $Cm(H_2O)_9^{3+}$	68	9 ± 0.5
Surfaces complexes	140 - 150	4 ± 0.5
Surface incorporation species pH < 10	~ 200	2.5 ± 0.5

References

[1] J.D.H. Donnay, D. Harker, A New Law of Crystal Morphology Extending the Law of Bravais, Am. Mineral. J. Earth Planet. Mater. 22 (1937) 446–467.

[2] H.-Y. Tseng, P.J. Heaney, T.C. Onstott, Characterization of lattice strain induced by neutron irradiation, Phys. Chem. Miner. 22 (1995) 399–405.

[3] C.F. Macrae, I. Sovago, S.J. Cottrell, P.T.A. Galek, P. McCabe, E. Pidcock, M. Platings, G.P. Shields, J.S. Stevens, M. Towler, P.A. Wood, Mercury 4.0 : from visualization to analysis, design and prediction, J. Appl. Crystallogr. 53 (2020) 226–235. https://doi.org/10.1107/S1600576719014092.

[4] J. Neumann, H. Brinkmann, S. Britz, J. Lützenkirchen, F. Bok, M. Stockmann, V. Brendler, T. Stumpf, M. Schmidt, A comprehensive study of the sorption mechanism and thermodynamics of f-element sorption onto K-feldspar, J. Colloid Interface Sci. 591 (2021) 490–499. https://doi.org/10.1016/j.jcis.2020.11.041.

[5] Z. Wang, D.E. Giammar, Mass Action Expressions for Bidentate Adsorption in Surface Complexation Modeling: Theory and Practice, Environ. Sci. Technol. 47 (2013) 3982–3996. https://doi.org/10.1021/es305180e.

[6] T. Stumpf, C. Hennig, A. Bauer, M.A. Denecke, T. Fanghänel, An EXAFS and TRLFS study of the sorption of trivalent actinides onto smectite and kaolinite, Radiochim. Acta. 92 (2004) 133–138. https://doi.org/10.1524/ract.92.3.133.30487.

[7] T. Kimura, G.R. Choppin, Y. Kato, Z. Yoshida, Determination of the Hydration Number of Cm(III) in Various Aqueous Solutions, Radiochim. Acta. 72 (1996) 61–64. https://doi.org/10.1524/ract.1996.72.2.61.

[8] H. Geckeis, J. Lützenkirchen, R. Polly, T. Rabung, M. Schmidt, Mineral-water interface reactions of actinides, Chem. Rev. 113 (2013) 1016–1062. https://doi.org/10.1021/cr300370h.

[9] M. Demnitz, K. Molodtsov, S. Schymura, A. Schierz, K. Müller, F. Jankovsky, V. Havlova, T. Stumpf, M. Schmidt, Effects of surface roughness and mineralogy on the sorption of Cm(III) on crystalline rock, J. Hazard. Mater. 423 (2022) 127006. https://doi.org/10.1016/j.jhazmat.2021.127006.